

Structure, energetics and kinetics of metallic grain boundary nano-voids and corresponding discrete model studied by multiscale and differential evolution simulations

Xiangyan Li^{a, 1}, Xiaolin Li^{a, b, 1}, Yange Zhang^{a, 1}, Yichun Xu^{a, *}, Xuebang Wu^{a, **}, Zhuoming Xie^a, Xianping Wang^a, B.C. Pan^c, C.S. Liu^a, Q.F. Fang^a, Jun-Ling Chen^d, G.-N. Luo^d, Zhiguang Wang^c

^a Key Laboratory of Materials Physics, Institute of Solid State Physics, HFIPS, Chinese Academy of Sciences, Hefei 230031, PR China

^b University of Science and Technology of China, Hefei 230026, PR China

^c Hefei National Laboratory for Physical Sciences at Microscale and Department of Physics, University of Science and Technology of China, Hefei 230026, PR China

^d Institute of Plasma Physics, HFIPS, Chinese Academy of Sciences, Hefei 230031, PR China

^e Institute of Modern Physics, Chinese Academy of Sciences, Lanzhou 730000, PR China

¹ These authors contributed to the work equally.

*, ** Correspondence authors: xuyichun@issp.ac.cn, xbwu@issp.ac.cn

Abstract

The behavior of nano-voids composed of vacancies (Vs) at grain boundaries (GBs) is fundamental to the design of the radiation tolerance of poly-crystalline metals (PCs) via GB engineering. In this study, based on differential evolution, a framework for determining the stable structure of GB nano-voids is developed. Combining the framework with multiscale simulations, we elucidate the vacancy-accumulation and GB void formation mechanism under irradiation. A GB-structure dependent picture is revealed. At special coincidence-site-lattice (CSL) GBs of $\Sigma 5(310)$ and $\Sigma 5(210)$ with a medium V-GB binding energy, the V could be reemitted from the GB and also has driving force to be clustered at the GB, developing particularly stable V-clusters from a linear configuration to a platelet and finally to three-dimensional void that has large strain fields in iron with small bulk modulus and a bulk-void alike structure in the GB with large bulk modulus. A group of vacancies reconstruct their positions during the growth. The ripening is also mediated by the mobility of small V-clusters in addition to free Vs. General high-angle and low-angle GBs trap Vs efficiently, where V-clusters only align one-dimensionally or hardly nucleate. Based on the bonding among the vacancies and their neighboring atoms of a nano-void, we propose a high-accuracy predictive linear energetic model applied to the nano-void both at the iron/molybdenum/tungsten GBs and in the grain interior. The model captures the anisotropic feature of a nano-void and reproduces the oscillated vacancy

energy level near a nano-void, showing distinct advantages over conventional continuum model and Wulff construction based energy model. Finally, the collective behavior of multiple GBs plays a role in the GB void formation. The present work offers fundamental mechanistic insights to GB nano-void formation and growth and sets a key step towards GB-void prevention in PCs by reducing the fraction of special CSL-GBs.

Keywords: grain boundary; multiscale simulation; differential evolution; nano-voids; discrete model

1. Introduction

Nano-voids composed of vacancies (V_s) and their clusters (V_n s), one of natural native defects prevalent in materials under radiation [1–4], deformation [5], annealing [6], and high hydrogen pressure [7], play an important role in determining materials properties and performance, e.g. swelling [1–4,8,9], creep [10,11], impurity retention [12–15], and intergranular corrosion [16]. Notably, the interface e.g. grain boundaries (GBs) serving as sinks for defects appears to act as nucleation sites for vacancies to coalesce. The voids (or cavities containing a limited amount of gaseous impurities) have been observed to form preferentially along GBs and at triple junctions in poly-crystalline metals (PCs) [2–4,10–14,16,17]. Since the GB voids observed as early as 1954 [17], the thermodynamic models for vacancy accumulation and void growth at GBs have been proposed [18,19]. However, the fundamental properties for the GB nano-void (e.g. its structure, energetics and kinetics) are still lacked except the properties of small V_n s in bulk metals [20–25], which necessitate thorough studies on the behavior of GB nano-voids.

Besides, the GB structure probably affects the nano-void formation mechanism in PCs [2–4,26,27] by providing different vacancy sink strengths and in-boundary properties of a nano-void. Experiments of the neutron and electron irradiations to PC Fe-15Cr-15Ni steel and PNC316 stainless steel at 749–775 K suggest that the void-denuded zone (VDZ) was formed only near a random GB, while voids were formed both in the grain interior and at coincidence site lattice (CSL) GBs [3]. In electron irradiation experiments at 573 K on Cu thin films [2], very few voids were observed around high-angle random GBs and low-angle GBs, while voids were preferentially observed to nucleate and grow in the regions with a high density of the coherent twin boundaries. The difference has been speculated to arise from the low sink strength of the low energy of the CSL-GBs [26]. On the other hand, however, the radiation response of NCs with high-density of GBs exhibits a scattered feature with respect to the GB character. For instance, VDZs were recently found to be independent of grain size, grain orientation, and GB misorientation angle in NC Fe [27]. Although the void size observed in these experiments is as large as tens of nanometers, the different large void formation

conditions are possibly related to the early period of the nano-void formation at the GBs with distinct structures. Therefore, the GB character complicates the GB nano-void behavior.

To obtain a full picture about a GB nano-void behavior, the first step is to find its stable structure, which acts as the basis of both the energetic and kinetic properties of the cluster. For this purpose, it in principle requires exploring the potential energy surface (PES) on the complex $3N$ -dimensional (N is the number of atoms in the system) configuration space and locating the global minimum of the PES. The challenging difficult exists as the cluster size is over a certain limit (e.g. 10 inaccessible to the enumerative algorithm) since the possible number of configurations increases exponentially with the cluster size. There already exist several methods for PES exploring, e.g. enumeration search methods [20–22,28,29] and the autonomous basin climbing method [30]. However, these methods may not be efficient enough to find the global minimum of the PES due to the exceptionally large configurational space of a V_n . Alternatively, in recent years, the biological intelligent global optimization algorithm e.g., genetic algorithm (GA), particle swarm optimization (PSO) and differential evolution (DE) have been proved to be successful in optimizing atomic clusters structure [31], crystal structure [32,33], interface/boundary structure [34] in the material science community and solving complex optimization problems in other fields [35]. The GA has been used to investigate the structure and stability of defects clusters in quite limited systems [36–38]. Compared to other group intelligence methods, the DE algorithm as one of heuristic group intelligence approaches to solve global optimization problems has advantages of simplicity, robustness and high performance [35,39].

To address the aforementioned challenge, in the present work, an approach in the framework of the DE was developed to find the stable configuration of a nano-void at Fe/Mo/W GBs and also in their grain interiors. The choice of the three model systems is based on the consideration of their identical crystal structure in addition to the nuclear industrial application of Fe/Mo/W as structural materials in nuclear reactors [26,40,41]. Besides, we also tried to relate the formation energy of a nano-void to its geometrical parameters (e.g. the bonding between V-V and the bonding between the V and the surrounding atoms). And

then, a predictive discrete model for the GB nano-void energetics was built. In addition, the kinetics of a V_n in the vicinity of the GB was investigated by using lattice kinetic Monte Carlo (LKMC) method [42]. Contrary to the object kinetic Monte Carlo (OKMC) with a pre-constructed rate catalog for the events [42], the rate catalog was rebuilt at every step of the LKMC. Furthermore, the energy barriers of all the transition paths of a nano-void were calculated in a parallel way by using nudge elastic band (NEB) method [43].

2. Simulation methods

2.1. Atomic GB models

The interatomic interaction between Fe atoms was described by the empirical potential proposed by Mendelev et al. as part of their embedded-atom method (EAM) (Potential 2 in Ref. [44]). The EAM potentials were also used to describe interatomic interaction in Mo [45] and W [46] (EAM4 in Ref. [46]). Since the vacancy behavior at the GB relates to the GB structure, multiple GBs were modeled in this work, including 44 symmetric tilt GBs of $[h\ k\ 0]/[0\ 0\ 1]$ with tilt axis of $[0\ 0\ 1]$ (index h and k varies within the range of $[2\ 13]$ and $[1\ 11]$, respectively). The misorientation angle (θ) for these GBs varies from 8.8 to 84.6°; Σ -value varies from 5 to 265. For comparison, several GBs with another tilt axis of $[1\ 1\ 0]$ were also modeled, including $\Sigma 3(1\ 1\ 1)/[1\ 1\ 0]$, $\Sigma 3(1\ 1\ 2)/[1\ 1\ 0]$, $\Sigma 9(1\ 1\ 4)/[1\ 1\ 0]$, $\Sigma 9(2\ 2\ 1)/[1\ 1\ 0]$, $\Sigma 11(1\ 1\ 3)/[1\ 1\ 0]$, and $\Sigma 11(3\ 3\ 2)/[1\ 1\ 0]$.

2.2. Details for searching the ground state configuration of a V_n at the GB by using the differential evolution (DE) algorithm

The life group intelligent algorithm DE [35,39] was employed to solve the global optimization issue related to finding the stable configuration of nano-void (Fig. 1(a)). The system was divided into two regions: the core region Reg1 where the V_n locates and its environment Reg2 (Fig. 1(b)). The space near a V_n in Reg1 was divided into mesh. Each site of the mesh denotes a state of the V composing a V_n in the un-relaxed space. Note that, the real structure of a V_n should be relaxed. Such notation of the V_n maps the relaxed space

to the un-relaxed space:

$$unrelaxed(V_n) \Leftrightarrow relaxed(V_n); R_{relaxed} = R_{unrelaxed} + \varepsilon, \quad (1)$$

where $R_{unrelaxed}$ and $R_{relaxed}$ is the V_n configuration before and after relaxation, respectively; ε is relaxation-induced displacement of a V_n . The individual V in a V_n before relaxation was considered to locate at a site near a lattice in the un-relaxed space (Eq. 1). For a V_n , the V composing the V_n was considered to locate at a crystal lattice site. Particularly, for the small V_n at the GB, the space mesh was restricted to the position sites of a single V in the V_n (the site with minimum V formation energy). Such restriction could significantly improve the search efficiency. The above approximation was found to be rational by comparing the configurations of the small V_n found via the DE method with that found by enumeration search method. Furthermore, multiple runs of the optimizer lead to the same stable configuration of a nano-void. For the large V_n , considering the possible expansion of the occupation range for the V in the V_n towards the bulk region from the GB, the mesh was also restricted to the region near the GB rather than only within the GB plane.

Based on above approximation, the problem of finding the global energy minimum on the PES of the V_n system containing NI sites in Reg1 was transformed into to a combinatorial problem of choosing n sites from NI and minimizing the system energy:

$$\min E = E(x), x = [x_1, x_2, \dots, x_n], x_i |_{i=1,n} \in [1, NI], \quad (2)$$

where x_i is an integer denoting the individual site label in Reg1. The DE was employed to solve this optimization problem over discrete integer space, including four steps of initialization, mutation, crossover, and selection, as illustrated in Fig. 1(c).

(a). Initialization

For a given calculated radius r of Reg1, the candidate sites set $C=\{C_1, C_2, \dots, C_{NI}\}$ in Reg1. Then, the basic parameters of the DE were set, including the population size Np , scale factor $Fscale$, and crossover probability Pcr . For each individual $x^j |_{j=1, 2, \dots, Np}$, it was assigned to n different integers randomly chosen

from [1, N1]. After testing, Np was set to be approximately 30–100 depending on the size of the cluster. $Fscale$ and Pcr were set to be 0.5 and 0.1, respectively. The convergence of the defects configuration with respect to r was checked by assigning r to be several values, e.g. 5, 10, 15 and 20 Å. If the obtained configuration does not change with increasing r , a small r is accepted. To reduce the number of candidate states for a V_n , the shape of Reg1 was also considered according to the possible shape of the V_n . For example, for a bulk V_n , Reg1 could be assigned to be spherical, while it is a rectangle at the GB given its preferred growth direction along the GB.

(b). Mutation

For each individual, a mutant vector ($h^j |_{j=1,2,\dots,Np}$) was generated according to (Fig. 1(c)):

$$h^j = \text{round}\{x^{r1} + Fscale \times (x^{r2} - x^{r3})\}, \quad (3)$$

where random indexes $r1, r2, r3$ were chosen from [1, Np] and *round* is a rounding off function. Since the V_n energy was optimized over integer space (Eq. 2), h^j in Eq. 3 was rounded off.

(c). Crossover

To increase the diversity of the population, crossover was introduced [39]. A trial vector $v^j = [v_1^j, v_2^j, \dots, v_n^j]$ was generated according to the following equation (Fig. 1(c)):

$$v_i^j = \begin{cases} h_i^j, & \text{if } \text{rand}(0,1) \leq Pcr \\ x_i^j, & \text{if } \text{rand}(0,1) > Pcr \end{cases}, \quad (4)$$

where i and j refers to the certain single defect in the cluster and individual in the population, respectively. Their values lie in the range of $i \in [1, n]$ and $j \in [1, Np]$, and $\text{rand}(0,1)$ is a uniform random number $\in [0, 1]$.

(d). Selection

Whether or not v^j replaces x^j as a new member of the population depends on the relative value of energy $E(v^j)$ and $E(x^j)$ (Fig. 1(c)). If $E(v^j)$ is smaller than $E(x^j)$, x^j is set to v^j . Here, the energy of each offspring was defined to the system energy, which could be readily transformed into the corresponding V_n formation energy. After decoding a certain offspring, we obtained the corresponding unrelaxed V_n configuration and created the V_n in an atomic system with an approximate size..

To improve the efficiency for searching the ground state of the defects cluster, several methods were adopted. First, the individual with two identical components was avoided by means of penalty function. Equivalently, as the two Vs in a V_n occupy the same state, the corresponding individual was given a very high energy. Second, the relaxation of a V_n expressed by an individual was performed every a specific steps. In principle, the system with a given initial rigid V_n has to be relaxed at 0 K or at a finite temperature to get the accurate energy for the V_n . Nevertheless, we found it is very time consuming as the system was relaxed at each step. To achieve a balance between the algorithm efficiency and accuracy, the system was only relaxed at a certain intervals (Fig. 1(d)), e.g. 20 steps in the present calculations. As relaxing the system, the conjugate gradient method was used to minimize the system energy at 0 K; the optimal time-step that leads to the maximal reduction in the system energy during each relaxation step was determined by using the golden section search method. In certain case, after relaxing the system with a V_n , a V in the V_n spontaneously jumps to other neighboring sites. Correspondingly, the mapping relation of the relaxed space to the un-relaxed space was modified. As finding the stable V_n configuration at the Fe GB, we found that the system has to be relaxed at a finite temperature, e.g. 300 K to obtain a low-energy V configuration. Third, to reduce the calculation time, the energies of all the individuals in the population were calculated in a parallel way. Finally, once the stable configuration V_{n0} has been obtained, a large V_n was optimized based on a small “core parts” V_{n0} (Fig. 1(b)). In this case, only the configuration V_{n-n0} was optimized by using the above DE algorithm (given the possible reconstruction of the V_n , $n0=n-k$ with $k>10$ or other larger value). We also checked the parameter range of each individual and made periodical adjustment of the parameter to ensure that each component of the individual lies in the range of $[1, N1]$. We also tried to express the energy of a V_n by its geometrical parameters, e.g. the bonding between V-V and the bonding between the V and the surrounding atoms. Once the express was obtained, the time-consuming relaxation of the system was avoided.

2.3. Energetics of V_n

To characterize the energetics of a V_n , we defined the V_n formation energy in a normal way as:

$$E_{V_n}^f = E_{V_n}^{tot} - E_0^{tot} + nE_{coh}, \quad (5)$$

where $E_{V_n}^{tot}$ is the energy of the system with a V_n , E_0^{tot} is the energy of a pure system without defects, E_{coh} is the cohesive energy per atom in the bulk of -4.122 eV. The clusters formation energy acts as an important parameter for determining the critical nucleation size of a cluster [26]. Particularly, $\Delta G_n^0 = -nk_B T \ln S_V + E_{V_n}^f$; $d\Delta G_n^0 / dn = -k_B T \ln S_V + \Delta E_{V_n}^f$ [26]. For a given temperature (T) and supersaturation concentration of the V (S_V), we can immediately obtain the critical nucleation size for a bulk void according to the energy level of a V near the void.

To characterize the binding tendency of a V to the nano-void, we also defined the V- V_n binding energy as:

$$E_b^{V-V_n} = E_V^f + E_{V_n}^f - E_{V_{n+1}}^f = E_V^f - \Delta E_{V_n}^f, \quad (6)$$

Considering that E_V^f is the energy level of the isolated V, the energy level of V near a cluster ($E_{V_n}^{V_n}$) was thus defined as:

$$E_{V_n}^{V_n} = E_{V_{n+1}}^f - E_{V_n}^f, \quad (7)$$

2.4. The kinetics of a nano-void near the GB determined by using lattice kinetic Monte Carlo (LKMC) method

Given the complex local atomic environment near the GB, the kinetics of a V in the vicinity of the GB was investigated by using LKMC method [42]. Contrary to the OKMC with a pre-constructed rate catalog for the events, in the present study, the rate catalog was rebuilt at every step of the LKMC. Each transition of the V_n from the current state was assumed to involve only one jump of the V to its first- and/or second-nearest neighbor position. For each transition identified, the transition path was optimized by using the standard nudge elastic band (NEB) method [43], as illustrated in Fig. 1(e). The energy barriers of all the transition paths were calculated in a parallel way. For a large nano-void, this could greatly improve the calculation speed. For the transition with the energy barrier of E_a , its transition rate was calculated via

$r = v_0 \exp(\frac{-E_a}{k_B T})$, where v_0 often in the range of $10^{12} - 10^{13} / s$ was assumed to be a fixed value of $10^{12}/s$. The

Boltzmann constant k_B has a value of 8.617×10^{-5} eV/K. T denotes absolute temperature. After the rate catalog was constructed, the transition pathway was selected according to the standard KMC algorithm, where the chosen probability of a transition is proportional to the transition rate. Then, one V of V_n jumps to the corresponding site.

The diffusion coefficient (D) of a vacancy cluster at an elevated temperature was determined as the proportionally factor between the mean squared displacement of the mass center of the void and the time. We found that a large V_n is easily trapped in a local basin at a low temperature. Therefore, the D of a V_n at a low temperature was extrapolated from the value at a high temperature once $\ln(D)$ and the reciprocal of temperature follows the Arrhenius relationship (Fig. 1(f)).

3. Results

3.1. Formation, trap, leakage and emission of the V near Fe GBs

We begin with investigating the behavior of single V near Fe GBs although the energetics of a V near Fe GBs has been studied systematically [47,48] and its kinetics near several GBs have also been studied [30,49–52]. By calculating the vacancy formation energy (E_{vf}^{GB}) at different sites near the GB, the site with the minimum E_{vf}^{GB} (mE_{vf}^{GB}) was found, which acts as the stable position of a V at the GB. The V distributes within several layers near the GB (supplementary Fig. S1). Figure 4(a) presents mE_{vf}^{GB} as a function of misorientation angle (θ). Although there is no obvious trend in mE_{vf}^{GB} with respect to θ , mE_{vf}^{GB} for some special low- Σ CSL-GBs (e.g. $\Sigma 5(2\ 1\ 0)/[0\ 0\ 1]$ and $\Sigma 5(3\ 1\ 0)/[0\ 0\ 1]$) is noticeably larger than that for the GBs nearby. The twin boundary of $\Sigma 3(1\ 1\ 2)/[1\ 1\ 0]$ has the highest mE_{vf}^{GB} . The low-angle GB with θ less than 15° owes mE_{vf}^{GB} larger than that for the high-angle GB nearby, while the low-angle GB with θ higher than 75° has mE_{vf}^{GB} smaller than that for the high-angle GB nearby. To reveal the distribution feature of the stable site for the V at the GB, the spacing between these V-trapping sites (as marked by symbol d in

supplementary Fig. S2(a)) is also presented in Fig. 2(a) as a function of θ . It can be seen that d basically exhibits a U-shape curve with θ , although it is scattered around a small value at the range of about 40–70°.

In addition to the above static interaction parameters of the V with/within the GB, the LKMC and OKMC methods were further employed to explore the dynamic behavior of the V near the GB at an elevated temperature (mainly high temperature). Given the anisotropic strain field near the GB, lattice kinetic Monte Carlo (LKMC) was firstly employed to study the V trapping by the GB and reveal its dependence on the local atomic environment. It was found that the V interacted with different GBs via three distinct mechanisms. The V near $\Sigma 5(3\ 1\ 0)/[0\ 0\ 1]$ firstly followed a random walk and then moved straightforward towards the GB; it finally located at the region of the several atomic layers near the GB (Fig. 2(b)). Such behavior was readily understood based on the bulk-like migration energy curve in the region far away from the GB and a downhill shape of the curve near the GB (Fig. 2(b)). Near the low-angle GB of $\Sigma 85(7\ 6\ 0)/[0\ 0\ 1]$ ($\theta=81.2^\circ$, effective $\theta=8.8^\circ$), the V in a wider range underwent a non-random walk drift towards the GB. The longer-ranged strain field near the low-angle GB could give rise to such behavior, consistent with the finding in Ref. [53] that the low-angle copper GB has large sink strength due to the effect of GB stress. However, as the misorientation angle further decreases (e.g. $\Sigma 1741(30\ 29\ 0)/[0\ 0\ 1]$ with effective value of 1.9°), the V near the region lying between the dislocation cores passed through the GB (Fig. 2(c)); similar phenomenon was observed for the V near $\Sigma 221(11\ 10\ 0)/[0\ 0\ 1]$ (supplementary Fig. S3). Such behavior was termed as the leakage effect. The V near the dislocation core of $\Sigma 1741(30\ 29\ 0)/[0\ 0\ 1]$ exhibited similar migration-trapping behavior to that near $\Sigma 85(7\ 6\ 0)/[0\ 0\ 1]$.

To measure the effect of the leakage on the V trapping, we further calculated the probability of a V moving away from the GB as a function of its distance normal to the GB at several GBs at 300 K (Fig. 2(d) and (e)). Initially, a V was put at the site in the bulk region about 25 Å from the GB. As there is no a sink near the V, the V has the same probability moving forward and backward. As expected, near a sink, the probability for the V moving away from the GB is less than 0.5 due to the trapping of the V by the GB. The

probability curves for the three GBs of $\Sigma 5(2\ 1\ 0)/[0\ 0\ 1]$, $\Sigma 5(3\ 1\ 0)/[0\ 0\ 1]$ and $\Sigma 3(1\ 1\ 2)/[1\ 1\ 0]$ are similar. However, the probability in a wider range is less than 0.5 for the low-angle GBs of $\Sigma 85(7\ 6\ 0)/[0\ 0\ 1]$ and $\Sigma 221(11\ 10\ 0)/[0\ 0\ 1]$. Yet, at an identical position near the GB, the moving-out probability for the V near the low-angle GBs (particularly near the GB of $\Sigma 1741(30\ 29\ 0)/[0\ 0\ 1]$) is larger than that near the high-angle GBs of $\Sigma 5(2\ 1\ 0)/[0\ 0\ 1]$, $\Sigma 5(3\ 1\ 0)/[0\ 0\ 1]$ and $\Sigma 3(1\ 1\ 2)/[1\ 1\ 0]$.

To investigate the segregation of the V/SIA to the GB and their re-emission out of the GB, object kinetic Monte Carlo (OKMC) method was also employed. For this purpose, the atomic processes embedded in the OKMC model only include the V/SIA migration near the GB, trapping by the GB and emission from the GB. Figure 2(f) presents the V motion trajectories near several GBs at several temperatures of 300, 400 and 600 K. At 300 K, the V was observed to be occasionally reemitted from the twin GB of $\Sigma 3(1\ 1\ 2)/[1\ 1\ 0]$ at 300 K after segregation to the GB (Fig. 2(f)). As temperature increases to 400 K, the V was frequently reemitted from the twin GB (Fig. 2(f)). At a high temperature of 600 K, the V trapped at the GB of $\Sigma 5(2\ 1\ 0)$ was found to be reemitted frequently out of the GB, while the emission is just an occasional event at the GB of $\Sigma 85(13\ 1\ 0)$ (Fig. 2(f)). The observed behavior is consistent with the magnitude of the V-GB binding energy in different GBs (the energy difference between E_{Vf}^{bulk} and E_{Vf}^{GB} in Fig. 2(a)). Therefore, the single V behavior near the GB is related to both the local GB structure and the V-GB interaction parameters (e.g. V-GB binding energy).

To further investigate the defect accumulation in NC/PC Fe, the stochastic cluster dynamics (SCD [54])/OKMC was used. The atomic processes within the GB were thus not allowed to occur, while in the grain interior all the atomic processes including diffusion, annihilation, binding, dissociation were allowed to occur. We calculated the trapping amount of the defects flowing into the GB. The typical values of V-GB binding energy (E_b or $E_{b_{trap}}$) were adopted to represent several types of GBs. For the twin boundary of $\Sigma 3(1\ 1\ 2)/[1\ 1\ 0]$, $E_{b_{trap}}$ for the V is 0.18 eV (Fig. 2(a)). For the special CSL-GB, $E_{b_{trap}}$ for the V in $\Sigma 5(2\ 1\ 0)$ of 0.49 eV was chosen as a representative value. For general high-angle GB or low-angle GB, $E_{b_{trap}}$ for the V

was given of 1.0 eV (the V-GB binding energy for $\Sigma 85(7\ 6\ 0)$). As the leakage process was taken into consideration, the leakage rate was given of 0.5. Figure 2(g) presents the net trapping flux of the V/SIAs as a function of radiation dose under the condition of $T=600\text{ K}$, $L=100\text{ nm}$ and $\tau=10^{-2}\text{ dpa}\cdot\text{s}^{-1}$. It can be seen that the accumulated V at the GB depend on $E_{b_{trap}}$ for the V. Compared to the other GBs, the net V concentration at the GB (C_V^{GB}) of $\Sigma 3(1\ 1\ 2)/[1\ 1\ 0]$ is exceptionally lower. It implies that the twin boundary could not trap defects efficiently. For a low dose (e.g. 0.005 dpa), there is no significant difference in the defect accumulation in the other GBs due to the rarity of defects emission at a low dose. The C_V^{GB} in the general GB/low angle GB is highest and becomes smaller as the V was leaked. The C_V^{GB} in the CSL-GB has an intermediate level in these systems. Therefore, the GB trapping efficiency for the V is sensitive to the V-GB binding energy. Consequently, as abundant Vs are present in the materials (e.g. under radiation), the quantity of Vs that segregate to the GB and compose the nano-void largely depends on the GB character.

3.2. V-clustering at Fe GB at high temperature

In addition to the relation of the trapping amount of the defects flowing into the GB to the local GB structure and V/SIA-GB binding energy, the determination of the defect accumulation at the GB also relies on the information of the defects within the GB, including the V kinetics at the GB, and V-V binding at the GB; of course, the V formation at the GB (Fig. 2(a)) also contributes the V accumulation within the GB (Fig. 2(g)), although it also determines the V segregation via providing the V -GB binding energy (Fig. 2(a)).

For the V kinetics at the GB, we calculated the V migration energy barrier at the GB by using the standard NEB method [43]. Figure 3(a) shows the V migration energy barrier (E_a) along two nonequivalent paths within the GB as a function of the misorientation angle θ . It suggests that E_a along one path is much lower than that along the other one, as indicated by the V migration potential energy surfaces along the two types of paths at the GBs of $\Sigma 5(3\ 1\ 0)$ and $\Sigma 85(7\ 6\ 0)$ (supplementary Fig. S4). It implies that the V prefers to migrate on a certain low-energy barrier direction. Such speculation is supported by the quasi-one dimensional trajectory of the V motion at the GB drawn from the OKMC simulations of the V/SIA diffusion

at the GB plane at 300 and 600 K (supplementary Fig. S5). Only at a high temperature, e.g. 600 K, the V/SIA at the special CSL-GBs of $\Sigma 5(2\ 1\ 0)/[0\ 0\ 1]$ and $\Sigma 5(3\ 1\ 0)/[0\ 0\ 1]$ and also $\Sigma 11(3\ 3\ 2)/[1\ 1\ 0]$ diffuses two dimensionally. In addition, E_a for the V along the GB exhibits U-shape dependence on θ . Basically, it could conclude that the V migration energy barrier is lower for the high-angle GBs compared to that for low-angle GBs. Different kinetics of the V at GBs may affect their clustering within the GB.

For V-V clustering/binding at the GB, we calculated V-V binding energy (E_b^{V-V}) (Eq. 6), which acts as an indicator for their clustering tendency. As shown in Fig. 3(b), E_b^{V-V} does not heavily depend on θ . Nonetheless, E_b^{V-V} in most investigated GBs is positive and higher than that for a Fe bulk V-V pair except that in several GBs with the tilt axis of $[1\ 1\ 0]$, indicating the attraction of Vs at the most GBs. Figure 3(c) presents the relation of E_b^{V-V} to E_{vf}^{GB} . A positive correlation between the two variables was observed, indicating that the GB with high E_{vf}^{GB} has more stable V clusters within itself. The formation energy of small V clusters and the corresponding binding energy of the V with the V-cluster were also further calculated in several typical GBs (Fig. 3(d) and 3(e)). It could be seen that E_{vn}^{GB} approximately show a linear relation to the cluster size of n , implying that the energy level of a V near the small V-cluster (the slope of the curve of the formation energy with respect to cluster size as defined by Eq. 7) basically remains a constant, different from the quick change of the V energetics near a bulk V_n [20]. Furthermore, $E_b^{V-V_n}$ exhibits a weak dependence on the cluster size of n , which arise from the linear configuration of the small V_n within the GB. Nonetheless, the capillary law describes a different relation of the cluster energy to its size [54]. The V that repels to each other will be annihilated or locate at the GB randomly. In face-centered cubic (fcc) systems [55], the Vs randomly generated at GBs induced the GB phase transformation. In the present work, the emphasis is on the alternative path for Vs at the GB as formatting V clusters and GB voids. These energetic results guide the modeling of the V accumulation at different GBs.

Given the net flux of the V into the GB and the Vs properties at the GB (Fig. 2(g)), the special CSL-GB acts as a candidate that probably develops a void structure under cumulative irradiation. Considering the V

attracting each other (e.g. the GB of $\Sigma 5(3\ 1\ 0)/[0\ 0\ 1]$), the trapped Vs could nucleate at the GB and grow to a GB void, as observed in experiments [3]. To explore the GB nano-void formation mechanism, the structure, morphology and energetics of nano-V clusters at Fe GB of $\Sigma 5(3\ 1\ 0)/[0\ 0\ 1]$ were further explored by using the DE method, although the structures of small V_n s ($n < 5$) in bulk Fe are well-known [20,26]. Figure 3(f) presents the energetics of the V_n at the GB. The energetics of the V_n have unique features. At the GB, from a single V to the 1D and then 2D configurations, the V has several typical energy levels corresponding to the specific folding configuration. The energy level oscillates with the size as n is larger than certain value, which is similar to the energetic behavior of small W bulk V_n/SIA_n in Ref. [56] ($n < 10$ for V_n and $n < 20$ for SIA_n). It arises from the formation of the interface between the defects and the atoms nearby. To understand the V_n configuration transition during its growth at the GB, a mathematical setting for examining this transition was proposed (illustrated in supplementary Fig. S6(h)). The mode was based on the bonding among defects and the atoms nearby with a core idea to increase the shared area of the defect clusters and further increase the bonding strength. The formation energy for a defect cluster V_{2n}/SIA_{2n} with a 1D and folding configuration is $E_1 = nE_{V/SIA}^{f1} - (2n-1)E_b^x + E_{s1}$ and $E_2 = nE_{V/SIA}^{f1} - [2(n-1)E_b^x + (2n-1)E_b^y] + E_{s2}$, respectively. Here, E_{s1}/E_{s2} is the energy increase in the configuration energy due to the formation of the interface between the cluster and the surrounding atoms; E_b^x and E_b^y denotes the V-V binding energy in the two directions parallel and nonparallel to tilt axis, respectively. We assume that each isolated V/SIA in the two configurations has the same formation energy of $E_{V/SIA}^{f1}, E_{V/SIA}^{f2}$ ($E_{V/SIA}^{f1} = E_{V/SIA}^{f2}$) and $E_{s1} = E_{s2}$. It is energetically favorable for the cluster to be folded as $E_1 \geq E_2$, which leads to the condition $2n \geq \frac{E_b^x}{E_b^y} + 1$. For

a different value of $E_{V/SIA}^{f1}, E_{V/SIA}^{f2}$, we have the condition $2n \geq \frac{E_b^x + E_b^y}{E_b^y + (E_{V/SIA}^{f1} - E_{V/SIA}^{f2})/2}$.

As displayed in Fig. 3(g), a single V resides at the GB in the form of V-I-V complexes (I denotes an interstitial) along $[3\ 1\ 0]$ with the SIA located nearly on the GB plane and acting as the center of the two Vs sitting at the two symmetric sites on the two GB sides (Fig. 3(g)). Such complex has energy lower than the

point-alike V structure found based on MS method [30,47–52]. Clusters V_2 – V_7 are composed of such V-I-V complex growing along $[0\ 0\ 1]$ (Fig. 3(g)). Then, V_8 is folded from 1D configuration along $[0\ 0\ 1]$ to a 2D platelet configuration composed of the same complex (Fig. 3(g) for V_8); two columns of $(V-I-V)_4$ complex are parallel to each other. During the above each stages of the V_n growth, the configuration folding decreases the V_n formation energy effectively (Fig. 3(f)). The mode of the V_n growth along $[0\ 0\ 1]$ and then undergoing folding repeats as n increases (Fig. 3(g)). As a result, V_n grows two dimensionally within the GB. Yet, the direction of the complex shifts from $[3\ 1\ 0]$ to $[1\ 1\ 1]$. In addition, it was also found that the lattice surrounding the V_n of the V-I-V complex is heavily strained approximately in the direction normal to the GB. With n increasing, more atoms contract towards the V_n . The maximal displacement is as large as $0.7\ \text{\AA}$. Compared to the small strain around a bulk spherical void [57] (the present EAM potential predicts the displacement around a bulk V_n is less than $0.1\ \text{\AA}$ after relaxation), the strain here observed near a GB V_n is significantly large, which may arise from the fact that the compress of a bulk 3D void needs more work compared to the compress of a 2D GB void. A bulk void is a neutral sink because of a lack of associated strain fields [8,26]. Therefore, the Fe-GB nano-void could act as a preferential sink. The strain field pattern also changes with n . The contraction strain field around the V_n in the form of V-I-V complex is probably an intrinsic feature in the 2D defect GB system. It may be related to the elastic modulus. Since the greater the elastic modulus, the greater the stress needed for a given strain, the V_n at a W CSL-GB may not have such low-energy V-I-V complex structure (the preliminary MS calculation of the two types of structures suggests that the V-I-V structure is unstable at W GB of $\Sigma 5(3\ 10\ 0)/[0\ 0\ 1]$).

As n further increases, the size of the cluster in the direction of $[0\ 0\ 1]$ is so large that the DE fails to optimize the V_n configuration as viewing the V_n as a collection of single Vs. We turn to optimize the GB structures with different columns of Vs along $[0\ 0\ 1]$ by the DE method. By such approximation, it implies an infinite size of the V_n in the $[0\ 0\ 1]$ direction, which may be rational only for a sufficiently large GB void. In this way, the optimized problem is finding the low energy configuration as creating N_c columns of Vs

from Mc columns of atoms along $[0\ 0\ 1]$ in the optimized region (equivalent number of Vs is $N_x \times N_c$ with N_x as the number atoms of a atom column along $[0\ 0\ 1]$). The optimization was carried out within a rectangle region with a maximal size of about 60 Å in the direction of $[1\ \bar{3}\ 0]$ and half-width of 10 Å in the direction of $[3\ 1\ 0]$ (the pink rectangle in supplementary Fig. S6(a)). It was found that for different values of N_c , the Vs at the GB developed to two types of structures. For a small $N_c < N_c^*$ (or equivalently the void height h in supplementary Fig. S6(c) is smaller than a specific value), the vacant region is unstable. During the structural relaxation of a GB system with a void, a group of atoms surrounding the region rearranged their positions, accompanied by the contraction of the atoms in the grain interior towards the GB. As a result, the metastable GB phase was formed (supplementary Fig. S6(a) and S6(b)), which has a different structural unit to the pure GB. Actually, the sign of the transition of a large V_n to the metastable GB phase also found during optimizing the V_n structure at the GB. For a large $N_c \geq N_c^*$, the vacant region no longer collapsed, but formed a stable GB void phase with naked low-energy surfaces decorated with steps (supplementary Fig. S6(c) and S6(d)). Meanwhile, the strain near the GB recovered from the contraction strain (supplementary Fig. S6(e) and S6(f)). The void structure at the GB is similar to that in a bulk iron.

We also found that the V-V binding energy at the GB and V kinetics at the GB are insufficient to determine the GB void morphology. For instance, the migration energy barrier of the single V along the GB and particularly V-V binding energy in some GBs ($\Sigma 5(2\ 1\ 0)/[0\ 0\ 1]$, $\Sigma 5(3\ 1\ 0)/[0\ 0\ 1]$, $\Sigma 13(5\ 1\ 0)/[0\ 0\ 1]$, $\Sigma 13(3\ 2\ 0)/[0\ 0\ 1]$, $\Sigma 25(4\ 3\ 0)$, $\Sigma 85(7\ 6\ 0)$, $\Sigma 85(13\ 1\ 0)/[0\ 0\ 1]$, $\Sigma 11(3\ 3\ 2)/[1\ 1\ 0]$) have similar level. As the input parameters to the OKMC model were chosen from these GBs, we obtained similar V_n nucleation/growth behavior for these GBs (supplementary Fig. S7). However, the DE calculation of the V_n configuration within theses GBs reveals two types of V_n morphology at the GB. Only at the GBs of $\Sigma 5(3\ 1\ 0)$ and $\Sigma 5(2\ 1\ 0)$ does the V_n have 1D-2D configuration, which further extends to the bulk region. The V_n at the remaining GBs possesses a 1D configuration along the tilt axis except that has V-V repulsion interaction. These results suggest the important role of the GB character in coarse-grained modeling defect accumulation

in PCs/NCs. Besides, the information of the large V_n structure plays a role in predicting damage structure evolution at the GB in addition to the energetic and kinetic properties of point defects and small clusters.

3.3. Structure and energetics of the W/Mo GB V_n

We have simulated V accumulation in Fe GBs (Figs. 2 and 3), finding that the behavior of clusters at the GB is essential to predicting radiation response of the GB. To explore the generalization of the results (mainly the V_n formation at the GB and its relation to the local GB structure), we further calculated the V_n configuration at Mo/W GBs by using the DE method. Figure 4(a–d) presents the V_n energetics at several Mo/W GBs (the V_n configuration in bulk W is shown in supplementary Fig. S8; some of V_n s in bulk Mo have identical configurations). It is found that the GBs could be divided into two categories according to their $E_{V_n f}^{GB}$ as separated by the orange dash line in Fig. 4(a) and (c). The $E_{V_n f}^{GB}$ at the GB of $\Sigma 5(3\ 1\ 0)$ and $\Sigma 5(2\ 1\ 0)/[0\ 0\ 1]$ is significantly higher than that at the other GBs. The single V formation energies at the two GBs are also higher than that at the other GBs. Furthermore, the GB V_n formation energy follows a different power law with respect to cluster size compared to that for a bulk V_n . It is well-known that the formation energy for a bulk 3D V_n has a dependence of $n^{2/3}$ [26] and the calculated values for bulk V_n in W/Mo indeed obey such relation. However, $E_{V_n f}^{GB}$ was found to be expressed by the linear combination of $n^{1/2}$ and n^1 , which ensures the convergence of $E_{V_n f}^{GB} \rightarrow E_{V_n f}^{bulk} \mid n > n_0 (1/2 < 2/3 < 1)$, implying that a GB V_n finally extends to the grain interior and becomes a bulk-alike void as its size is sufficiently large (supplementary Fig. S6(c) and S6(d)). Besides, the coefficient for $n^{1/2}$ is much larger than that for n^1 (e.g. for V_n at W GB of $\Sigma 5(3\ 1\ 0)$, the two coefficients for $n^{1/2}$ and n^1 are 4.21 and 0.46, respectively), suggesting that a small V_n at the GB could be considered as a planar loop. The differentiation formation energy was clearly divided into two stages (Fig. 4(b) and (d)). Both $\Delta E_{V_n f}^{GB}$ and $\Delta E_{V_n f}^{bulk}$ decline quickly from 1 to about 5 and then oscillate between several typical levels. Such behavior could not be captured by the above n-power law continuum model which predicts that $\Delta E_{V_n f}^{bulk/GB} = \Delta E_{V_n f}^{bulk/GB} [n^{2/3} - (n-1)^{2/3}] / [2^{2/3} - 1]$ (note that in Ref. [20], $E_b(n) = E_f + [E_b(2) - E_f][n^{2/3} - (n-1)^{2/3}] / [2^{2/3} - 1]$; here we have modified some symbols according to Eqs.

(6) and (7)). In the following section, we will see that the V_n with a low V energy level is more thermodynamically stable which serves as void nucleation center (the n that satisfies $k_B T \ln S_V = \Delta E_{V_n f}^{bulk}$ determines the critical nucleation size [26]).

Correspondingly, the V_n configurations at the investigated nine GBs are clearly classified to two categories. In the W/Mo GBs of $\Sigma 5(3\ 1\ 0)/[0\ 0\ 1]$ and $\Sigma 5(2\ 1\ 0)/[0\ 0\ 1]$ (Fig. 4(e–h)), the V_n initially adopts a linear configuration along the tilt axis on one side of the GB (note that the small V_n at the two Fe GBs has a V-I-V complex configuration). The V_n occupies the stable site for a single V at the GB, except for V_2 at W GB of $\Sigma 5(2\ 1\ 0)/[0\ 0\ 1]$ (Fig. 4(f)). Then, the V_n develops to a 3D structure centered at the GB plane, occupying additional sites in addition to the V stable site. During the development of a large V_n , it did not always grow on the basis of V_{n-1} , the reconstruction of the V_n was accompanied (e.g. from V_4 to V_5 in Fig. 4(e) and for some bulk V_n s in iron as suggested in supplementary Fig. S9). For some special clusters with a certain n , its configuration is mirror-symmetric about the GB plane, which may arise from the intrinsic symmetry of the CSL-GB. With the highly symmetric cluster as a center, the newly arriving V s were absorbed at one side of the center until another symmetric V_n was formed. Through such growth process, the V_n extends in the three directions. We also found that the V_n at the GB of $\Sigma 5(3\ 1\ 0)/[0\ 0\ 1]$ more frequently develops to a symmetric structure than the V_n at the GB of $\Sigma 5(2\ 1\ 0)/[0\ 0\ 1]$. In the remaining GBs, the V_n was aligned along the tilt axis one-dimensionally with a V-I-V complex configuration.

We then examined the relation of the GB V_n morphology (3D versus 1D structure and point structure versus V-I-V complex) to the local GB structure. We note that a bulk V has equivalent neighboring sites with identical vacancy formation energy. Besides, the GB V_n with cluster formation energy close to bulk values possesses a 3D configuration. Therefore, the configuration of the V_n could be related to the fluctuation degree of the potential energy surface near the V_n . Figure 5(a) presents the V formation energy distribution at several GBs of W. Indeed, in the GBs of $\Sigma 5(3\ 1\ 0)/[0\ 0\ 1]$ and $\Sigma 5(2\ 1\ 0)/[0\ 0\ 1]$, the stable sites for the V with minimum formation energy are very near to each other not only in the direction along the tilt axis but

also in the other direction. In the other GBs, the stable sites are aligned along the tilt axis. Furthermore, there are several atom columns with high V formation energy between the stable sites in the other direction along the GB. To further measure the flat degree of the potential energy surface at the GB, we calculated the standard error of vacancy formation energy (E_V^f) for the group of GB atoms with low E_V^f as a function of the GB type in W. As shown in Fig. 5(b), the standard error well indicates two categories of the GBs with 3D/1D V_n morphology. A small error implies that the V prefers to condense along a certain direction, forming a 1D structure, while a large error implies that the local environment varies gently and the V_n easily extends towards the surrounding sites via a 3D manner.

In addition to the 3D/1D configuration of the V_n at the GB, we further analyzed the strain around a GB V_n and its relation to the GB structure (Fig. 5(c–e)). We found that the configuration of the V at the GB as a point or V-I-V complex is related to both the GB excess volume and the bulk modulus. The system either with low bulk modulus (e.g. Fe) or with small excess volume (e.g. W/Mo) has low energy V configuration in the form of V-I-V complex, while the V behaves like a point at the GB lattice site with large excess volume and high bulk modulus.

3.4. Discrete model for the energetics of a GB V_n

As mentioned in the above section, the continuum model fails to capture the oscillated feature in the differential formation energy. Consequently, the thermal stability of a nano-void could not be well described by the model; the further formation and growth mechanism of the nano-void predicted by the model could be different to the real path. Next, we built discrete energetic models for GB V_n by using the locally structural information of a cluster rather than only using the cluster size as in the continuum model. As observing the configuration of the V_n (Fig. 6(a)), we found that the Vs within the V_n were naturally connected by a series of bonds. Considering the interaction among Vs of the V_n and interaction between the V_n with the surrounding atoms, the V_n formation energy was represented as the linear combination of the V-V and V-atom bonding: $E_{V_n f}^{bulk/GB} = \sum_i (n_{V-V_i} I_{V-V_i} + n_{V-Ai} J_{V-Ai})$ (Fig. 6(b)), where the sum extends to all the

neighboring V-V and V-atom pairs; n_{V-Vi} is the number of i -th nearest V-V neighboring pair, I_{V-Vi} is the bonding strength for the V-V pair, n_{V-Ai} is the number of i -th nearest V-atom neighboring pair, and J_{V-Ai} is the bonding strength for the V-atom pair. Note that, for a specific neighboring distance, I_{V-Vi} and J_{V-Ai} are constants. Such a linear model leads to the representation of the first-order differentiation of the formation energy as $\Delta E_{V_{nf}}^{bulk/GB} = \sum_i (\Delta n_{V-Vi} I_{V-Vi} + \Delta n_{V-Ai} J_{V-Ai})$. For the bulk V_n , the V-V pair was restricted to the third nearest neighbor, while V-A pair was only set to be the first nearest neighbor. For the GB V_n , the all the V-V and V-A neighboring distances were firstly calculated. According to their distribution, the typical values were chosen. In the discrete model, the parameters I_{V-Vi} and J_{V-Ai} could be obtained by fitting the calculated void formation energy to its structural variables n_{V-Vi} and n_{V-Ai} . By considering the contribution of different neighboring V-V and V-atom pairs, the model naturally distinguishes the anisotropic feature of a nano-void with different facets. Besides, the model gives a discrete expression for the surface energy per area. The iron $\langle 1\ 0\ 0 \rangle$ surface is taken as an example. For this surface, $E_{V_{nf}} = n(2I_{V-V2} + 4J_{V-A1})$, while the surface area is $S = ns_0$ with s_0 as the area of an atom. We could obtain the surface energy per area as $\gamma = E_{V_{nf}} / S = (2I_{V-V2} + 4J_{V-A1}) / s_0$. Such model gives γ a value of 1.71J/m^2 , well consistent with the calculated value of 1.78 J/m^2 by using molecular statics.

As presented in Fig. 6(c), such discrete bonding formula could describe both formation energy and its first-order differentiation with a very high precision (e.g. the maximum residual error for Fe bulk V_n formation energy is as low as 0.05 eV in the discrete model based on V-V and V-atom bonding, which is as high as 1.0 eV in the continuum model). Consequently, the oscillation in the V energy level (Fig. 6(c)) was well reproduced by the discrete model, while the continuum model [54] neglecting the topology of the cluster and its structural relation with the underlying lattice fails in describing such oscillation feature (Fig. 6(c)). In addition, the discrete model also naturally predicts a limited number of energy levels of the V near a void since the Δn_{V-Vi} and Δn_{V-Ai} present in its energetic model have limited number of integer values. Besides, we could understand the discrete energy level of V based on such discrete model. A specific energy level in

Fig. 6(c) corresponds to a local atomic environment that a new V occupies near a V_n . Figure 6(e–g) suggests that the discrete model also applies to describe the energetics of the GB V_n . Magana et al. [58] also proposed a modified Ising model to describe the clustering of Vs in bulk silicon voids. Although their model succeeded in describing the oscillation of V-voids binding energy, the model precision is lower than our model (e.g. the predicted binding energy for the V with V_1 - V_3 is identical in Fig. 1 in Ref. [58]). Our discrete model also has predictive property. With the discrete model, the energy of the population in DE optimization of the V_n structure (section 2.2) was directly calculated by only counting the number of neighboring V-V and V-atom pairs. Compared to the relaxation of the system with a V_n , the optimization speed was significantly improved. For a large V_n (e.g. $n > 100$), such discrete model based calculation of the V_n energy could efficiently leads to the ground state of a void.

The alternative discrete model was built based on the geometrical surface units of a V_n . A bulk Fe V_n contains two types of geometrical surface units with area of s_a and s_b , respectively (as illustrated in Fig. 6(a) by V_{15}). The V_n formation energy was thus represented by $E_{V_n f}^{bulk} = \sum_i n_i \gamma_i s_i$, where n_i is the number of surface unit i , γ_i is its surface energy per area and s_i is its area. But such model has a precision of only 0.7 eV to describe the bulk V_n formation energy. The precision is too low to describe the differentiation formation energy that is on the order of 0–3 eV (Fig. 4(b) and (d)). Actually, a similar expression was employed in the Wull construction based energetic model for a void polyhedron [59], where the ratio of the surface energy pre area of different surfaces of the void determines the equilibrium shape of the void. The failing of these models to describe the energy of a nano-void arises from the neglected contribution of the junction between different surfaces to the total energy of the void. Compared to a very limited fraction of the junction in a meso-/macro-scopic void, the junction in a nano-void could play an important role in its energy. In a more approximated model based on spherical assumption of the shape of a void, the energy of a void is expressed as $E_{V_n f}^{bulk/GB} = \gamma s$ [26], where γ is its surface energy per area and s is its area. Such model neglects the anisotropic surface tension for different surfaces of the void in addition to the aforementioned the role of the

junction in the total energy of the void. Therefore, these surface-based models do not apply to describe the formation energy of a nano-void, particularly its differential formation energy.

3.5. Stability of a GB V_n

We finally investigated the thermodynamic and dynamic stability of a GB V_n . A V_n at a high temperature will dissociate. Correspondingly, the time for the V_n to emit a V at an elevated temperature was used to characterize its thermodynamic stability (supplementary Fig. S10(a)). An emitted V from the GB V_n could locate at the GB or in the bulk (the corresponding time is t_1/t_2). Due to the low V energy level at the GB (Fig. 2(a), Fig. 4(b) and 4(d)) and migration energy barrier along the GB (Fig. 3(a)), a smaller time (t_l) was employed to characterize the lifetime of a V_n at the interested GBs of $\Sigma 5(3\ 1\ 0)$ and $\Sigma 5(2\ 1\ 0)$ where the V_n develops three dimensionally (Fig. 3(g) and Fig. 4(e-h)). As for the dynamic stability of the GB V_n , the diffusion coefficient of the V_n (D) within the GB was selected as an indicator. A small D implies that the V_n remains immobile at a specific temperature. The D was calculated either directly via calculating the mean squared displacements of the V_n at the GB at an elevated temperature or via the extrapolation from the high-temperature Arrhenius diffusion coefficient (D) (Fig. 1(f) and supplementary Fig. S10(b), section 2.4).

Figure 7(a-c) shows the lifetime for a GB/bulk V_n in Fe/Mo/W. We found that the lifetime of a V_n depends heavily on the cluster size and its location (GB or bulk) in addition to temperature. It can be seen that although the lifetime for a V_n exhibits an increasing trend with the cluster size, the increasing trend is non-monotonous. Some V_n s with the special size (e.g. V_6 , V_8 and V_{15} , V_{59} in bulk Fe; V_{24} , V_{31} at Mo GB of $\Sigma 5(3\ 1\ 0)/[0\ 0\ 1]$; V_{13} and V_{21} at W GB of $\Sigma 5(2\ 1\ 0)/[0\ 0\ 1]$) have longer lifetime compared to the adjacent ones, acting as stable centers for void nucleation/growth. With the temperature increasing, the lifetime for both GB and bulk V_n reduces greatly, indicating the instability of the V_n at a high temperature thermodynamically. Yet, V_{59} in bulk Fe is still stable at a high temperature of 700 K, as indicated by a lifetime of over one day. The thermodynamic stability may be related to the structural symmetry of a V_n (Fig. 4(e-h), Fig. 6(a)). At a low temperature of 300 K, most of V_n s are stable except V_1 and V_2 . At an

intermediate temperature of 500 K, only large cluster ($n>25$) and some small V_n s (V_6 , V_8 , V_{13} , V_{14} , V_{15}) are stable thermodynamically. We also found that the lifetime for a GB V_n at a certain temperature is much smaller than that for a bulk V_n , implying that the bulk V_n is much stable than a GB V_n . In other words, the GB V_n has to nucleate either on a large V_n or under high supersaturation of V s at the GB, while a relatively small V_n could act as the nucleation sites for a bulk V_n . Of course, the gaseous impurities also stabilize a void [7–9].

Next, the dynamic stability of the V_n was obtained based on its D . Figure 7(d–f) displays the D for small V_n at the GB/bulk in Fe/Mo/W. We found that the D for a V_n exhibits a decreasing trend with n , which however does not decrease monotonically with n and shows a discrete feature. The lower the temperature is, the more obvious the discretization in the D is (e.g. V_6 and V_8 have exceptionally small D at 300 K). The small V_n still has a considerable mobility, as suggested by its moderate D . Similar relation of the cluster mobility to its structural symmetry was also found for bulk V_n in iron (supplementary Fig. S11). The theoretical formula of a bubble D derived based on the surface diffusion [60] (the D is proportional to the reciprocal of R^4 or $n^{4/3}$, where R is the radius of a bubble) does not apply to a V_n , particularly at a low temperature. The D for a GB V_n is not necessarily higher than that for a bulk V_n , although GBs have been considered as high-diffusivity paths [26]. For the GBs of $\Sigma 5(3\ 1\ 0)$ and $\Sigma 5(2\ 1\ 0)$ in Mo and GB of $\Sigma 5(2\ 1\ 0)$ in W, the GB V_n has a higher D compared to that for a bulk V_n , while the diffusion is slower along the Fe/W GB of $\Sigma 5(3\ 1\ 0)$ than in bulk Fe/W.

Considering both the thermodynamic and dynamic stability, the stability of a V_n is summarized, as illustrated in Fig. 7(f). At regime 1, the V_n is unstable both thermodynamically and kinetically (e.g. V_1 – V_5 at Mo GB of $\Sigma 5(3\ 1\ 0)$). The V_n with $n < n_0$ falls into such regime, which contributes to the growth of a void via its dissociation ($n > 1$) and diffusion. Such mechanism is different to the classic Ostwald ripening mechanism, where the large void grows only by the dissociation of small voids. Besides, the n_0 for bulk V_n is larger than that for a GB V_n , implying that a GB void quickly becomes ripened compared to a bulk void. At regime 2,

the V_n with $n=n^*>n_l$ acts as a stable center for the V to nucleate both thermodynamically and dynamically (e.g. V_{15} and V_{59} in Fe bulk and V_{13} and V_{21} at W GB of $\Sigma 5(2\ 1\ 0)$). At regime 3, the V_n ($n_0 < n < n_l$) is thermodynamically stable but could diffuse (e.g. bulk V_6 and V_8) to bind with other stable clusters. At regime 4, the V_n is immobile but could dissociate, which could be the large cluster composed of some unstable branches and a stable center.

4. Discussion

4.1. Effect of the discretization nature of the energetics and kinetics on void formation and ripening

We have shown that both the energetics and kinetics of the GB/bulk void exhibit a discretization feature (Fig. 3(e) and 3(f), Fig. 4(b) and 4(d), Fig. 6(c) and 6(e–g), Fig. 7, supplementary Figs. S10 and S11). Next we examine its effect on the void formation and ripening by using different binding models for the description of vacancy agglomeration. In the first case, we compared the model predicted average void size during SCD annealing to that detected in positron annihilation spectroscopy experiments on neutron irradiated single-crystal bcc Fe [61]. Results suggest that our discrete model leads to the average cluster size of 9 after annealing the system initially containing a concatenation of 10^{25} m^{-3} Vs at 50°C for 50 minutes (Fig. 8(a)), consistent with the experimental value, while the continuum model underestimates the average size. The further annealing simulations at high temperatures of 150°C and 250°C suggest that small clusters also drive the ripening process of the void in addition to free vacancies (Fig. 8(b) and 8(c)). For the GB void formation, there are no direct experiments as benchmarks to simulations. Yet, results indicate the significant differences in cluster size distribution predicted by the two different models (Fig. 8(d) and 8(e)), while the difference is small at a low temperature (Fig. 8(d)). The discrete model correctly reproduces the formation of particularly stable cluster centers, as predicted by the V energy level near a V_n (Fig. 3(f), Fig. 4(b) and 4(d)) and also the cluster lifetime (Fig. 7(a–c)). Meanwhile, the maximum cluster size is smaller predicted by the continuum model than by the discrete model due to the underestimated energy level of the V near the V_n .

with low thermal stability (Fig. 3(e), Fig. 6(e–g)).

4.2. Vacancy accumulation and void formation mechanism at GBs under radiation

At a high temperature in a PC system, the GB response mechanism to irradiation depends on the GB structure [2–4,26,27]. The first determinate factor of the GB radiation response is the quantity of the Vs segregated to the GB, which is related to both the V-GB interaction strength and the distribution of the trapping sites at the GB (Fig. 2). Such factor dominates the vacancy concentration near the GB and further formation of the void-denuded zone near the GB. As illustrated in Fig. 9, the V energy level at the GB ($E1$ – $E4$) varies significantly with the GB type (Fig. 2(a), Fig. 4(b) and (d)). These energy levels define two decisive variables of the V-GB binding energy (Eb_{trap}) and the energetic driving force of the Vs to be clustered at the GB ($Eb_{clustering}$). Depending on the magnitude of Eb_{trap} , the V either permanently resides at the GB after segregation or is reemitted out of the GB (Fig. 9). The reemission of the trapped V at the GB is closely associated with the GB structure due to the scattered but relative small Eb_{trap} for the V in different GBs (Fig. 2). The experimentally observed difference in the radiation response near different types of GBs, e.g. void-denuded zone formation and non-denuded zone mainly relies on the difference in the V-GB binding strength in these GBs. The twin boundary could not effectively trap the V due to the high V energy level ($E1$) and exceptionally small Eb_{trap} (Fig. 2(a), Fig. 9); no sufficient defects could survive at the GB (Fig. 2(g)). The low-angle GB and high-angle general GB could effectively absorb Vs from the grain interior (Fig. 2(a), 2(e), 2(f)) due to the low energy level of the V at the GB ($E3$ and $E4$) and the corresponding large Eb_{trap} (Fig. 2(a)). The larger strain field near the low-angle GB also promotes the trapping of the V (Fig. 2(b) and 2(c)). Depending on the distribution of the trapping site along the GB, the trapping efficiency of the extremely low-angle GB is however lower compared to the general high-angle GB due to the leakage of the defects from the bulk-like region between the dislocation-centers (Fig. 2(d) and 2(g)). The special CSL-GB has an intermediate V energy level (Fig. 2(a), Fig. 9); correspondingly, the net quantity of Vs trapped at the GB lies between the values for the twin boundary and low-angle/general high-angle GBs (Fig. 2(g)).

The additional determinate factor of the GB radiation response is their topology at the GB after the segregation. The relevant defects properties within the GB include migration style along the GB, migration energy barrier, binding energy between defects, and nucleation and growth processes of the V_n at the GB. The parameters for the nucleation (e.g. V-V_n binding energy) are scattered with misorientation angle (Fig. 3(b)), while the structure and kinetics of small V_n depend on the GB structure (Figs. 3–5). The Vs collected at the GBs of $\Sigma 5(3\ 1\ 0)$ and $\Sigma 5(2\ 1\ 0)$ develops to a compact 3D structure from a linear structure (Figs. 3 and 3) via the migration of the single V (Fig. 3(a)) or/and small V_n (Fig. 7(d–f)). The Vs at the other GB either could not bind with each other due to the repulsion between Vs or develop to a 1D structure lying within the GB with low thermodynamic stability (Fig. 3(b)). Besides, the growth of a GB void largely relies on E_{vf}^{GB} . A bulk V segregates to the GB energetically driven by the energy difference between E_{vf}^{bulk} and E_{vf}^{GB} ($E_{b_{trap}}$). Once the segregated V contributes to the growth of the stable GB void, it is energetically driven by the energy difference between E_{vf}^{GB} and $E_{vf}^{GB\ void}$ ($E_{b_{clustering}}$). Near a void of a certain size, $E_{vf}^{GB\ void}$ remains a small scattered value (Fig. 3(f)) and is close to zero averagely as predicted by the capillary law [26,54]. Therefore, $E_{b_{trap}}$ and $E_{b_{clustering}}$ is mutually restricted by the equation of $E_{b_{trap}} + E_{b_{clustering}} \leq E_{vf}^{bulk}$. Meanwhile, compared to other GBs, the special CSL-GB has a relative small $E_{b_{trap}}$ (Fig. 2(a) and also as illustrated in Fig. 9). As a result, the defects accumulated at the low-angle GB and general high-angle GB with high $E_{b_{trap}}$ would have a small energetic driving force of $E_{b_{clustering}}$ to grow (Fig. 9). In contrast, the defects collected at the special CSL-GB have a large $E_{b_{clustering}}$ to further grow (Fig. 9). The Vs could finally agglomerate to the 3D GB void that is visible under TEM [3].

4.3. Effect of the coupling of grain size with GB character on vacancy accumulation at the GB

The results in Figs. 2–8 are obtained in a single bi-crystal model. The real material contains the GB network composed of different types of GBs, connected by the triple junctions as observed in experiments [2,27,62]. Under certain kinetic conditions, radiation defects trapped at the GB could migrate along the GB network (the small migration energy barrier in Fig. 3(a) provides the kinetic condition), flowing about from

one GB to another. Equivalently, the potential wells with different depths are connected (as illustrated in Fig. 9 by the light yellow curve). The V coming from the grain interior initially occupy the wells with a high V energy level tend to move towards the well with a low V energy level (as illustrated in Fig. 9 by the yellow arrow). Correspondingly, the V accumulation in the material would be the collective consequence of multiple GBs.

To support such speculation, we designed a system containing two sinks A and B with two energy levels of the V, as illustrated in supplementary Fig. S12(a). Sinks A and B could exchange defects with each other via emission, diffusion and trap processes in the OKMC model (supplementary Fig. S12(b)). The V was randomly produced in the two sinks at a rate. We found that the Vs in A with a high energy level flowed towards B before its reemission out of A. Moreover, the shorter the distance between A and B is, the more Vs finally flowed to B (supplementary Fig. S12(b)), implying the grain size effect in the process. Another SCD model where only the emission and trap processes were allowed to occur also confirmed the flow of Vs from A to B (supplementary Fig. S12(c)). Initially, the A and B were loaded with an equal number of Vs. As time passed, the Vs flowed from A to B with a lower energy level, as indicated by the decrease in the V percent in A and the increase in the V percent in B (supplementary Fig. S12(c)). Therefore, before the V could be emitted out of a local GB parts with small V-GB binding energy (or equivalently a high E_{Vf}^{GB}), the V finds its more stable site at the other GB (Fig. 2(a)). We termed this emission-inhibition behavior as the defects cruise within the GB, which significantly affects the V accumulation and distribution in a PC under irradiation.

Next, the cruise condition was derived. As the time for V emission out of the GB ($t_{\text{emission}} = t_0 e^{(E_{Vf}^{\text{bulk}} - E_{Vf}^{GB} + E_{Vm}^{\text{bulk}})/(k_B T)}$) is longer than that for the defects moving along the GB to find a low energy site in the other GB nearby ($t_{\text{cruise}} = L_m^2 / (2D) = L^2 / (2D) = L^2 / (2D_0 e^{-E_{Vm}^{GB}/(k_B T)})$) with L_m as the distance that a V has wandered during its diffusion process at the GB; here it was given of a typical value of grain size L), the V emission is inhibited. This leads to the following emission-inhibition condition:

$L^2 e^{(E_{Vf}^{GB} + E_{Vm}^{GB})/(k_B T)} < 2D_0 t_0 e^{(E_{Vf}^{bulk} + E_{Vm}^{bulk})/(k_B T)}$. The physical insight manifestly encompassed in this equation is the coupling of the grain size (L) with the GB character (the characterization parameters E_{Vf}^{GB} and E_{Vm}^{GB}). Specifically, the cruise is easy to occur within the GB with a small E_V^f and E_{Vm}^{GB} for a given L or under the condition of a small L for a given GB with certain V properties (supplementary Table S1). For a large L and large E_V^f and E_{Vm}^{GB} , the emission tends to occur compared to the cruise (supplementary Table S1). For the other combinations of L , E_{Vf}^{GB} and E_{Vm}^{GB} , it is not easy to arrive at a definitive conclusion on the relative rate of cruise and emission (supplementary Table S1). For instance, the V at $\Sigma 5(2\ 10)/[0\ 0\ 1]$ tends to cruise along the GB at 600 K as the grain size is less than 500 nm due to its small migration energy barrier of 0.36 eV, although its formation energy is as high as 1.22 eV (supplementary Table S1).

The V cruise along the GB network would affect the relation of radiation-performance to the V-GB binding strength in PCs/NCs. The V emission plays a critical role in distinguishing the role of different GBs under irradiation by reducing the trapping efficiency of the GB for the defects in addition to the leakage (Fig. 2(g)). As the V emission is inhibited under a certain condition, a definitive energy-space relation of the magnitude of the V-GB binding energy to the formation of the void-denuded zone near the corresponding GB (e.g. a large V-GB binding energy corresponds to the formation of the void-denuded zone) is broken. This brings about the uncertainty about the GB binding strength and radiation performance, as observed in NC Fe where different GBs of the same type exhibit difference in radiation performance at a high temperature [27]. Therefore, at a certain material parameter and radiation condition, the radiation-microstructure at a local region (particularly for a small grain size) is probably the result of collective behaviors of multiple GBs within a segment of the GB network.

4.4. Implication of the V accumulation mechanism for designing the radiation resistance of a nano-structured metal

Reducing the grain size is a well-known strategy for enhancing the radiation resistance of a poly-crystal metal. Our results provide new atomic insight into radiation damage reduction in NC metals from the view

of the GB structure and have implications for designing and optimizing radiation-resistant NCs. The present work reveals several compromise approaches to tailor radiation performance of NCs and juggle the stability of the GB by taking advantage of the character of the GB itself.

To improve the trapping efficiency of the defects by the GB, it qualitatively requires the increase in the binding energy of the defects with the GB. For example, the twin boundary binds with the V/SIA weakly compared to other GBs, and consequently the defect accumulation rate in the grain interior is larger than in other GBs at a high temperature due to the V/SIA emission from the GB. To obtain better radiation resistance of NCs at a high T , the fraction of the twin boundary in the nano-structured system should be decreased. At a high radiation dose, the special CSL-GB is not recommended to have a large volume fraction, given the formation of the 3D void at the GB under irradiation (Figs. 3 and 4) because of the large energetic driving for the V to be clustered due to the relative high energy level of the V at the GB (Fig. 2(a)) and the flat vacancy potential energy surface at the GB (Fig. 5(a)). Besides, the void would further trap gaseous impurities, forming bubble and promoting boundary embattlement [8,63,64]. The general high-angle GB is recommended to give high volume fraction to improve the radiation-tolerance considering the difficulty in the GB voids formation. The large Eb_{trap} gives rise to the high trapping capacity of the GB for the defects. Moreover, together with small $Eb_{clustering}$, the trapped defects are hard to nucleate at the GB or difficult to grow. Meanwhile, in view of the coupling of the grain size with the GB character (supplementary Fig. S12) and Table S1), the GB trapping efficiency is enhanced via the flow of the defects trapped at a CSL-GB with high defects formation energy to the general high-angle/low-angle GBs with low defects formation energy. Therefore, for high temperature application, the general GB with large defects-GB binding energy is suggested to have a large fraction together with a certain fraction of the CSL GB that stabilizes the GB network and meanwhile absorbs defects via defects transport towards the general GB, as pointed in Ref. [2].

There is a balance between the trapping and leakage of the defects near low-angle GBs. Although the low-angle GB shows good trapping ability for the defects (Fig. 2), the leakage effect emerges in the

extremely low-angle GB, resulting in a low trapping efficiency in such system (Fig. 2(g)). Therefore, the system with a high fraction of the low-angle GB with appropriate angle should have high radiation resistance.

5. Conclusions

To sum up, based on the differential evolution, we developed a framework for determining the stable structure of a nano-void. Combining the framework with multiscale simulations, the structure, energetics and kinetics of both the point vacancy (V) and vacancy-cluster at iron (Fe), tungsten (W) and molybdenum (Mo) grain boundaries (GBs) have been systematically studied. We found that the void formation condition at GBs is closely related to the GB structure. At special coincidence-site-lattice (CSL) GBs of $\Sigma 5(3\ 1\ 0)$ and $\Sigma 5(2\ 1\ 0)$, the V-GB binding energy is at a medium level, which although causes the V to be reemitted from the GB but also provides the driving force V-V binding at the GB. V-clusters with discrete size act as stable nucleation centers, developing from a linear configuration to a platelet and finally to a three-dimensional void with low thermodynamic stability. The growth is accompanied by the structural reconstruction of a group of vacancies. The small vacancy clusters with a relative mobility also contribute to the void formation in addition to the free Vs. The morphology of the V-clusters at the GB relates to both the excess volume and bulk modulus. General high-angle and low-angle GBs trap Vs efficiently (the V could be leaked from the exceptionally low-angle GB), where V-clusters only align one-dimensionally or hardly nucleate. A high-accuracy predictive linear model for the energetics of a nano-void both at the Fe/Mo/W GBs and in the grain interiors has been proposed based on the bonding among the vacancies and neighboring atoms of a nano-void. The model captures the anisotropic feature of a nano-void and reproduces the oscillation in the vacancy energy level near a nano-void, exhibiting superb advantages over widely used continuum model and Wulff construction based model for the energy of a meso-/macroscopic void. Considering the flow of Vs from the GB with high V formation energy towards the GB with low formation energy, the collective

behavior of GB networks plays a role in GB void formation. To render the poly-crystal Fe/W/Mo more radiation-resistant at a high temperature, the general GB with large defects-GB binding energy is suggested to have a large fraction. The present work provides new knowledge in understanding the GB void formation and enables sound basis for tailoring poly-crystal's radiation resistance to void formation by reducing the fraction of special CSL-GBs.

Declaration of Competing Interest

The authors declare that they have no known competing financial interests or personal relationships that could have appeared to influence the work reported in this paper.

Acknowledgments

This work was supported by the National Key Research and Development Program of China (Grant Nos.: 2022YFE03110000, 2019YFE03110200, 2018YFE0308102), the National Natural Science Foundation of China (Nos.: 12192282, 11735015, 51871207, 52071314, U1967211, 52171084, U1832206), and Foundation of President of Hefei Institutes of Physical Science, Chinese Academy of Sciences (No: YZJJQY202203). Numerical computations were performed on Hefei advanced computing center and the Center for Computation Science, Hefei Institutes of Physical Sciences.

References

- [1] T. Tanaka, K. Oka, S. Ohnuki, S. Yamashita, T. Suda, S. Watanabe, E. Wakai, Synergistic effect of helium and hydrogen for defect evolution under multi-ion irradiation of Fe-Cr ferritic alloys. *J. Nucl. Mater.* 329–333 (2004) 294–298.
- [2] T. LaGrange, K. Arakawa, H. Yasuda, M. Kumar, Preferential void formation at crystallographically ordered grain boundaries in nanotwinned copper thin films. *Acta Mater.* 96 (2015) 284–291.
- [3] Y. Sekio, S. Yamashita, N. Sakaguchi, H. Takahashi, Void denuded zone formation for Fe-15Cr-15Ni steel and PNC316 stainless under neutron and electron irradiations. *J. Nucl. Mater.* 458 (2015) 355–360.
- [4] W.Z. Han, M.J. Demkowicz, E.G. Fu, Y.Q. Wang, A. Misra, Effect of grain boundary character on sink efficiency. *Acta Mater.* 60 (2012) 6341–6351.
- [5] G. Righi, C.J. Ruestes, C.V. Stan, S.J. Ali, R.E. Rudd, M. Kawasaki, H.-S. Park, M.A. Meyers, Towards the ultimate strength of iron: spalling through laser shock. *Acta Mater.* 215 (2021) 117072.
- [6] F.A. Selim, M.H. Weber, D. Solodovnikov, K.G. Lynn, Nature of native defects in ZnO. *Phys. Rev. Lett.* 99 (2007) 085502.
- [7] Y. Fukai, N. Okuma, Formation of superabundant vacancies in Pd hydride under high hydrogen pressures. *Phys. Rev. Lett.* 73 (1994) 1640.
- [8] A. Bhattacharya, S.J. Zinkle, Cavity swelling in irradiated materials R.J. Konings, R.E. Stoller (Eds.), *Comprehensive Nuclear Materials* (2nd ed.), Elsevier, Oxford (2020) 406–455.
- [9] L. Mansur, E. Lee, Theoretical basis for unified analysis of experimental data and design of swelling-resistant alloys. *J. Nucl. Mater.* 179 (1991) 105–110.
- [10] L. Zhang, Y. Shibuta, C. Lu, X. Huang, Interaction between nano-voids and migrating grain boundary by molecular dynamics simulation. *Acta Mater.* 173 (2019) 206–224.
- [11] M.E. Kassner, T.A. Hayes, Creep cavitation in metals. *Int. J. Plasticity* 19 (2003) 1715–1748.
- [12] Q.-Y. Ren, Y.-H. Li, H.-B. Zhou, Z.-Z. Li, L. Cheng, G.-H. Lu, Characterization of the energetics and configurations of hydrogen in vacancy clusters in tungsten. *Nucl. Fusion* 59 (2019) 106032.
- [13] J.M. Polfus, O.M. Løvvik, R. Bredesen, T. Peters, Hydrogen induced vacancy clustering and void formation mechanisms at grain boundaries in palladium. *Acta Mater.* 195 (2020) 708–719.
- [14] M.A. Tschopp, F. Gao, K.N. Solanki, He-V cluster nucleation and growth in α -Fe grain boundaries. *Acta Mater.* 124 (2017) 544–555.
- [15] K. Czelej, M.R. Zemła, P. Kamińska, P. Śpiewak, K.J. Kurzydłowski, Clustering of hydrogen, phosphorus, and vacancies in diamond: A density functional theory analysis. *Phys. Rev. Lett.* 98 (2018) 075208.
- [16] L. Jiang, K. Wang, B. Leng, X.-X. Ye, S.-J. Chen, R.-D. Liu, J.-P. Liang, C.-W. Li, Z.-J. Li, Tellurium

segregation-induced intergranular corrosion of GH353 alloys in molten salt. *Corros. Sci.* 194 (2022) 109944.

- [17] J.N. Greenwood, D.R. Miller, J.W. Suiter, Intergranular cavitation in stressed metals. *Acta Metall.* 2 (1954) 250–258.
- [18] R. Raj, M.F. Ashby, Intergranular fracture at elevated temperature. *Acta Metall.* 23 (1975) 653–842.
- [19] D. Hull, D.E. Rimmer, The growth of grain-boundary voids under stress. *Phil. Mag.* 4 (1959) 673.
- [20] C.-C. Fu, J.D. Torre, F. Willaime, J.-L. Bocquet, A. Barbu, Multiscale modeling of defect kinetics in irradiated iron. *Nat. Mater.* 4 (2005) 68–74.
- [21] T. Ahlgren, K. Heinola, N. Juslin, A. Huronen, Bond-order potential for point and extended defect simulations in tungsten. *J. Appl. Phys.* 107 (2010) 033516.
- [22] J.R. Beeler, R.A. Johnson, Vacancy clusters in α -iron. *Phys. Rev.* 156 (1967) 677–684.
- [23] K. Morishita, R. Sugano, B.D. Wirth, T. Diaz de la Rubia, Thermal stability of helium-vacancy clusters in iron. *Nucl. Instrum. Meth. B* 202 (2003) 76–81.
- [24] V.A. Borodin, P.V. Vladimirov, Diffusion coefficients and thermal stability of small helium-vacancy clusters in iron. *J. Nucl. Mater.* 362 (2007) 161–166.
- [25] V.A. Borodin, P.V. Vladimirov, Kinetic properties of small He-vacancy clusters in iron. *J. Nucl. Mater.* 386–388 (2009) 106–108.
- [26] G.S. Was, *Fundamentals of Radiation Materials Science: Metals and Alloys*, 1st ed, Springer, New York, Berlin, Heidelberg, 2007.
- [27] O. El-Atwani, J.E. Nathaniel II, A.C. Leff, B.R. Muntifering, J.K. Baldwin, K. Hattar, M.L. Taheri, The role of grain size in He bubble formation: Implications for swelling resistance. *J. Nucl. Mater.* 484 (2017) 236–244.
- [28] X. Li, G. Duan, Y. Xu, Y. Zhang, W. Liu, C.S. Liu, Y. Liang, J.-L. Chen, G.-N. Luo, Annihilating vacancies via dynamics reflection and emission of interstitials in nano-crystal tungsten. *Nucl. Fusion* 57 (2017) 116055.
- [29] L.-L. Niu, Y. Zhang, X. Shu, S. Jin, H.-B. Zhou, F. Gao, G.-H. Lu, Interplay between intrinsic point defects and low-angle grain boundary in bcc tungsten: effects of local stress field. *J. Phys.: Condens. Matter* 27 (2015) 255007.
- [30] X.-Z. Tang, Y.-F. Guo, Y. Fan, S. Yip, B. Yildiz, Interstitial emission at grain boundary in nanolayered α -Fe. *Acta Mater.* 105 (2016) 147–154.
- [31] R.L. Johnston, Evolving better nanoparticles: Genetic algorithms for optimising cluster geometries. *Dalton Trans.* (2003) 4193–4207.
- [32] M.D. Wolf, Uzi. Landman, Genetic algorithms for structural cluster optimization. *J. Phys. Chem. A* 102 (1998) 6129–6137.
- [33] Y. Wang, J. Lv, L. Zhu, Y. Ma, Crystal structure prediction via particle-swarm optimization. *Phys. Rev. B* 82 (2010) 094116.
- [34] Q. Zhu, A. Samanta, B. Li, R.E. Rudd, T. Frolov, Predicting phase behavior of grain boundaries with evolutionary search and machine learning. *Nat. Commun.* 9 (2018) 467.

- [35] K.R. Opara, J. Arabas, Differential evolution: A survey of theoretical analyses. *Swarm Evol. Comput.* 44 (2019) 546–558.
- [36] A. Kaczmarowski, S. Yang, I. Szlufarska, D. Morgan, Genetic algorithm optimization of defect clusters in crystalline materials. *Comput. Mater. Sci.* 98 (2015) 234–244.
- [37] H. Ko, A. Kaczmarowski, I. Szlufarska, D. Morgan, Optimization of self-interstitial clusters in 3C-SiC with genetic algorithm. *J. Nucl. Mater.* 492 (2017) 62–73.
- [38] L. Wang, X. Shu, G. Lu, F. Gao, Energetics and structures of hydrogen-vacancy clusters in tungsten based on genetic algorithm, *Sci. China* 61 (2018) 107022.
- [39] R. Storn, K. Price, Differential evolution – A simple and efficient heuristic for global optimization over continuous spaces. *J. Global Optim.* 11 (1997) 341–359.
- [40] S.J. Zinkle, L.L. Snead, Designing radiation resistance in materials for fusion energy. *Annu. Rev. Mater. Res.* 44 (2014) 241–67.
- [41] S.J. Zinkle, G.S. Was, Materials challenges in nuclear energy. *Acta Mater.* 61 (2013) 735–758.
- [42] K.E. Sickafus, E.A. Kotomin, B.P. Uberuaga, *Radiation effects in solids*, Springer, 2007.
- [43] G. Henkelman, H. Jónsson, Improved tangent estimate in the nudged elastic band method for finding minimum energy paths and saddle points. *J. Chem. Phys.* 113 (2000) 9978–9985.
- [44] M.I. Mendelev, S. Han, D.J. Srolovitz, G.J. Ackland, D.Y. Sun, M. Asta, Development of new interatomic potentials appropriate for crystalline and liquid iron. *Philos. Mag.* 83 (2003) 3977–3994.
- [45] G.J. Ackland, R. Thetford, An improved N-body semi-empirical model for body-centred cubic transition metals. *Philos. Mag. A* 56 (1987) 15–30.
- [46] M-C. Marinica, L. Ventelon, M.R. Gilbert, L. Proville, S.L. Dudarev, J. Marian, G. Bencteux, F. Willaime, Interatomic potentials for modelling radiation defects and dislocations in tungsten. *J. Phys.: Condens. Matter* 25 (2013) 395502.
- [47] M. Tschopp, K.N. Solanki, F. Gao, X. Sun, M.A. Khaleel, M.F. Horstemeyer, Probing grain boundary sink strength at the nanoscale: Energetics and length scales of vacancy and interstitial absorption by grain boundaries in α -Fe. *Phys. Rev. B* 85 (2012) 064108.
- [48] M.A. Tschopp, M.F. Horstemeyer, F. Gao, X. Sun, M. Khaleel, Energetic driving force for preferential binding of self-interstitial atoms to Fe grain boundaries over vacancies. *Scripta Mater.* 64 (2011) 908–911.
- [49] D. Chen, J. Wang, T. Chen, L. Shao, Defect annihilation at grain boundaries in α -Fe. *Sci. Rep.* 3 (2013) 1450.
- [50] X. Li, W. Liu, Y. Xu, C.S. Liu, Q.F. Fang, B.C. Pan, J.-L. Chen, G.-N. Luo, Z. Wang, Principal physical parameters characterizing the interactions between irradiation-induced point defects and several tilt symmetric grain boundaries in Fe, Mo and W. *J. Nucl. Mater.* 444 (2014) 229–236.
- [51] X. Li, W. Liu, Y. Xu, C.S. Liu, B.C. Pan, Y. Liang, Q.F. Fang, J.-L. Chen, G.-N. Luo, G.-H. Lu, Z. Wang, Radiation resistance of nano-crystalline iron: Coupling of the fundamental segregation process and the annihilation of interstitials

and vacancies near the grain boundaries. *Acta Mater.* 109 (2016) 115–127.

- [52] X. Li, Y. Xu, G. Duan, J. Sun, C. Hao, Y. Zhang, W. Liu, C.S. Liu, Q.F. Fang, On the possibility of universal interstitial emission induced annihilation in metallic nanostructures. *J. Nucl. Mater.* 500 (2018) 199–212.
- [53] C. Jiang, N. Swaminathan, J. Deng, D. Morgan, I. Szlufarska, Effect of grain boundary stresses on sink strength. *Mater. Res. Lett.* 2 (2014) 100.
- [54] A. Dunn, R. Dingreville, E. Martínez, L. Capolungo, Identification of dominant damage accumulation processes at grain boundaries during irradiation in nanocrystalline α -Fe: A statistical study. *Acta Mater.* 110 (2016) 306–323.
- [55] T. Frolov, D.L. Olmsted, M. Asta, Y. Mishin, Structural phase transformations in metallic grain boundaries. *Nat. Commun.* 4 (2013) 1899.
- [56] L.-L. Niu, Y. Zhang, X. Shu, S. Jin, H.-B. Zhou, F. Gao, G.-H. Lu, Interplay between intrinsic point defects and low-angle grain boundary in bcc tungsten: effects of local stress field. *J. Phys.: Condens. Matter* 27 (2015) 255007.
- [57] M.R. Gilbert, S.L. Dudarev, P.M. Derlet, D.G. Pettifor, Structure and metastability of mesoscopic vacancy and interstitial loop defects in iron and tungsten. *J. Phys.: Condens. Matter* 20 (2008) 345214.
- [58] A. La Magna, S. Coffa, L. Colombo, Role of extended vacancy-vacancy interaction on the ripening of voids in silicon. *Phys. Rev. Lett.* 82 (1999) 1720.
- [59] G. Wulff, On the question of speed of growth and dissolution of crystal surfaces, *Z. Krist.* 34 (1901) 449 .
- [60] G.W. Greenwood, M.V. Speight, An analysis of the diffusion of fission gas bubbles and its effect on the behaviour of reactor fuels. *J. Nucl. Mater.* 10 (1963) 140.
- [61] M. Eldrup, B.N. Singh, Study of defect annealing behaviour in neutron irradiated Cu and Fe using positron annihilation and electrical conductivity. *J. Nucl. Mater.* 276 (2000) 269–277.
- [62] O. El-Atwani, K. Hattar, J.A. Hinks, G. Greaves, S.S. Harilal, A. Hassanein, Helium bubble formation in ultrafine and nanocrystalline tungsten under different extreme conditions. *J. Nucl. Mater.* 458 (2015) 216–223.
- [63] P. Lejcek, Grain boundary segregation in metals, Springer, Verlag, 2010.
- [64] I. Adlakha, K.N. Solanki, Atomic-scale investigation of triple junction role on defects binding energetics and structural stability in α -Fe. *Acta Mater.* 118 (2016) 64–76.

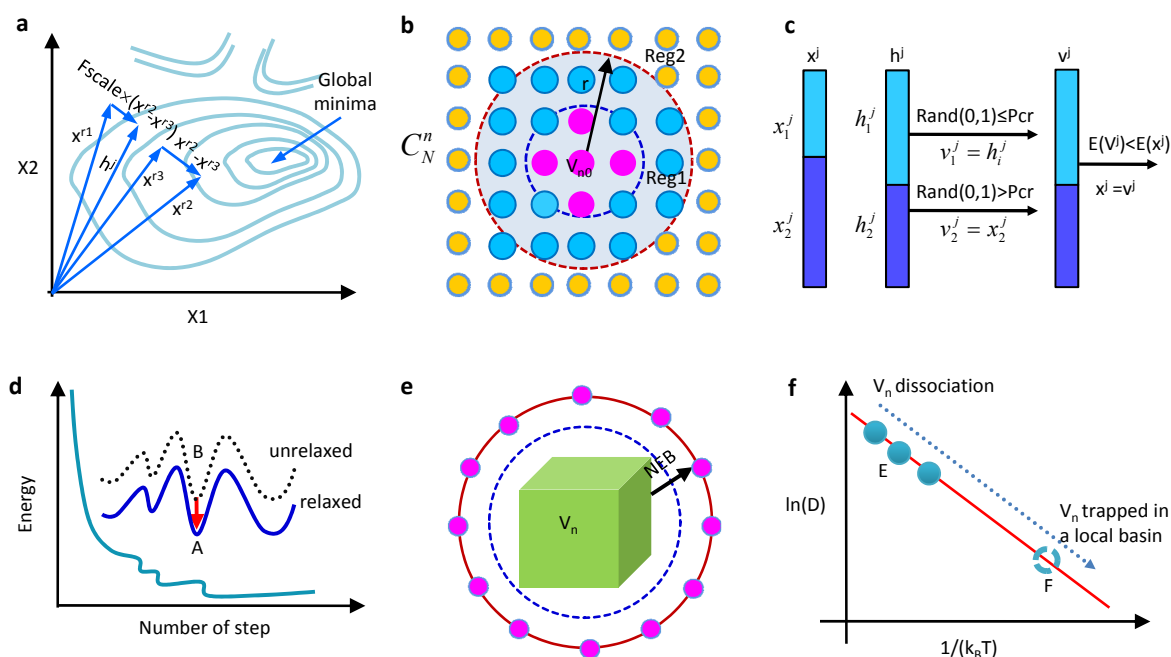


Fig. 1. (a–d) Illustration of the differential evolution (DE) method for finding the ground state structures of the V_n . Here, the potential energy surface is for a di-V cluster. In (c), the cross-mutation is exemplified by the case of V_2 . (e) Illustration of the geometry model for calculating V_n kinetics. The green cubic denotes a V_n , while the pink spheres represent the neighboring sites of the V_n . The arrow denotes one migration path of the Vs composing the V_n . (f) Illustration of the extrapolating V_n diffusion coefficient (D) at a high temperature (T) to that at a low T . k_B is Boltzmann constant.

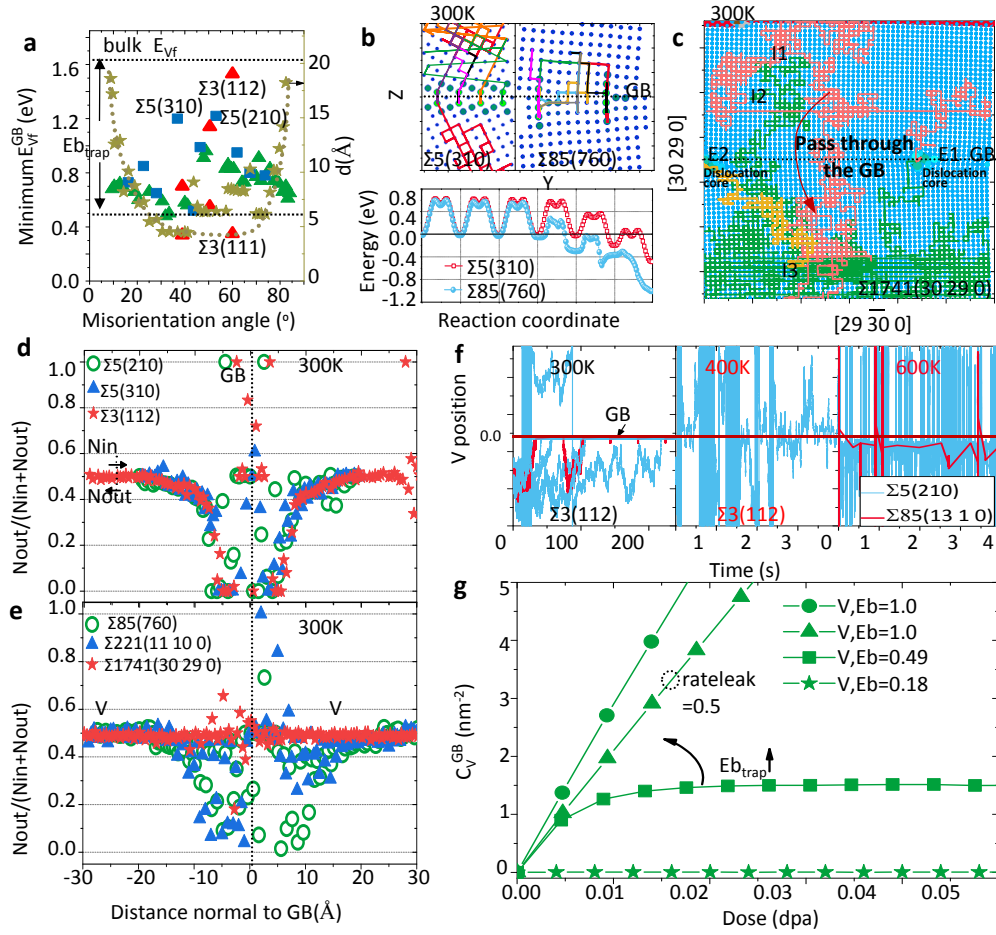


Fig. 2. (a) The basic energetics of the V at the Fe GBs. Here, the right axis is for the spacing between trapping sites at the GB. (b) The typical V motion trajectories near the GBs of $\Sigma 5(310)/[001]$ and $\Sigma 85(760)/[001]$ at 300 K drawn from lattice kinetic Monte Carlo (LKMC) simulation of the V diffusion near the GB. The horizontal line indicates the GB position. Axis Z is normal to the GB plane, while axis Y is parallel to the GB plane. For $\Sigma 5(310)/[001]$, Y and Z is along $[1\bar{3}0]$ and $[310]$, respectively, while for $\Sigma 85(760)/[001]$ Y and Z is along $[6\bar{7}0]$ and $[760]$, respectively. (c) Several motion trajectories of the V near a low-angle GB of $\Sigma 1741(30290)/[001]$ at 300K. Here, symbols I1, I2 and I3 mark three initial sites of the introduced V, while E1 and E2 mark the final trapping sites. (d) and (e) The probability of a V moving away from the GB as a function of its distance normal to the GB at several GBs at 300 K. Initially, a V was put at the site about 25 Å from the GB. (f) The motion trajectories of a V near the GBs at 300, 400 and 600K drawn from object kinetic Monte Carlo (OKMC) simulations of the V behavior near the GB. Initially, the V is about 6 nm away from the GBs. The horizontal line indicates the GB position. (g) The V concentration at

the GB (C_V^{GB}) as a function of radiation dose at 600 K for typical values of the V-GB binding energy (E_b or $E_{b_{trap}}$), as marked in (a). Here, $rate_{leak}$ denotes the leakage rate of the V from the GB.

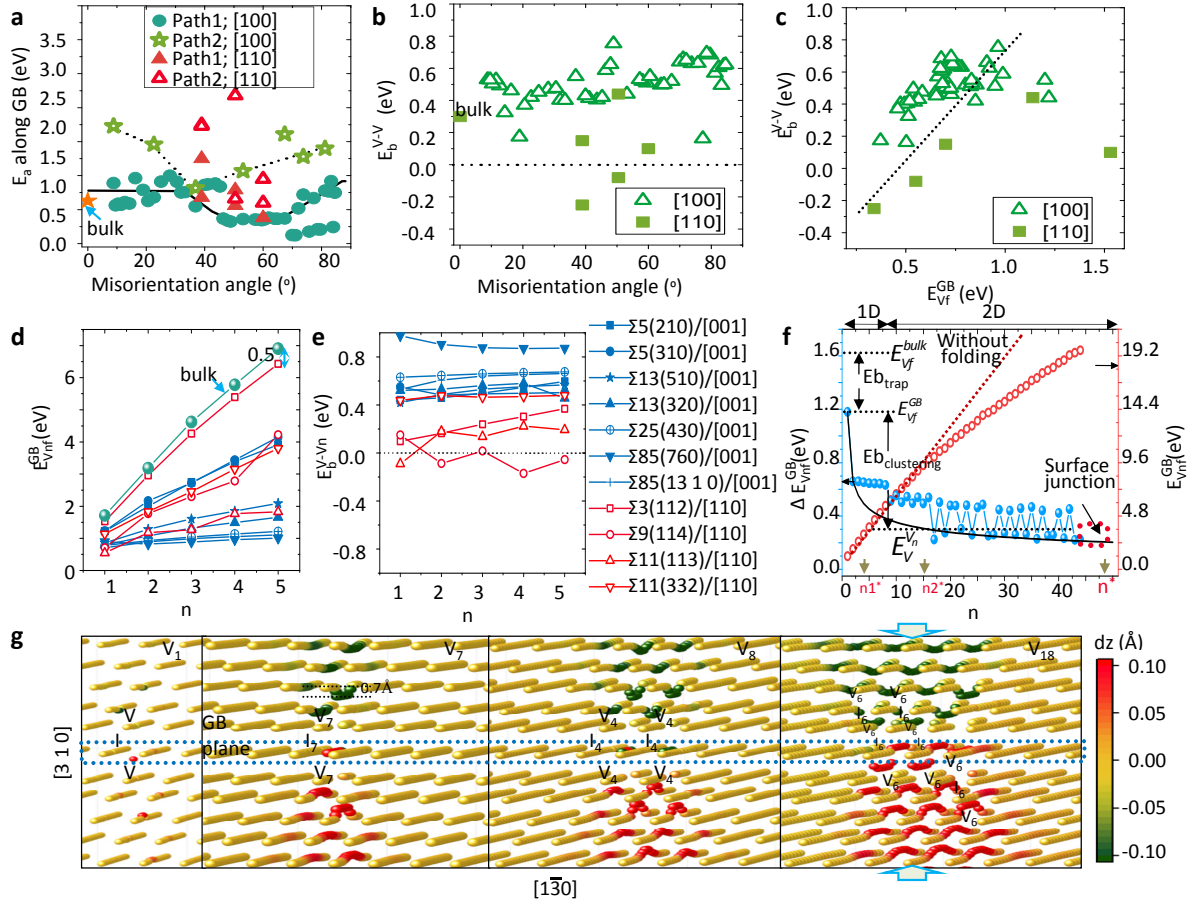


Fig. 3. (a) The V migration energy barriers (E_a) along two paths within the Fe GBs. (b) The V-V binding energy (E_b^{V-V}) at the GB as a function of the misorientation angle. (c) The relation of the V-V binding energy to the minimum V formation energy at the GB. (d) The V-cluster formation energy (E_{Vnf}^{GB}) as a function of the cluster size n . (e) The binding energy of the V-V $_n$ (E_b^{V-Vn}) at the GBs as a function of n . (f) The V $_n$ formation energy (E_{Vnf}^{GB}) (right axis) and its one-order difference ($E_{Vn+1f}^{GB} - E_{Vnf}^{GB}$) (left axis) as a function of n within the GB. Here, $n1^*$ the critical cluster sizes for the V $_n$ structural transition from a 1D configuration aligned along [0 0 1] tilt axis to a 2D configuration with two columns of Vs parallel to the tilt axis. Similarly, $n2^*$ is the critical cluster size for the V $_n$ transition from a two-column configuration to a three-column configuration along the tilt axis. Here, the black line indicates the result of E_{Vnf}^{GB} predicted by the continuum model. (g) The ground state structures of several V $_n$ s within Σ5(3 1 0)/[0 0 1]. Here, dz is atomic displacement along [3 1 0].

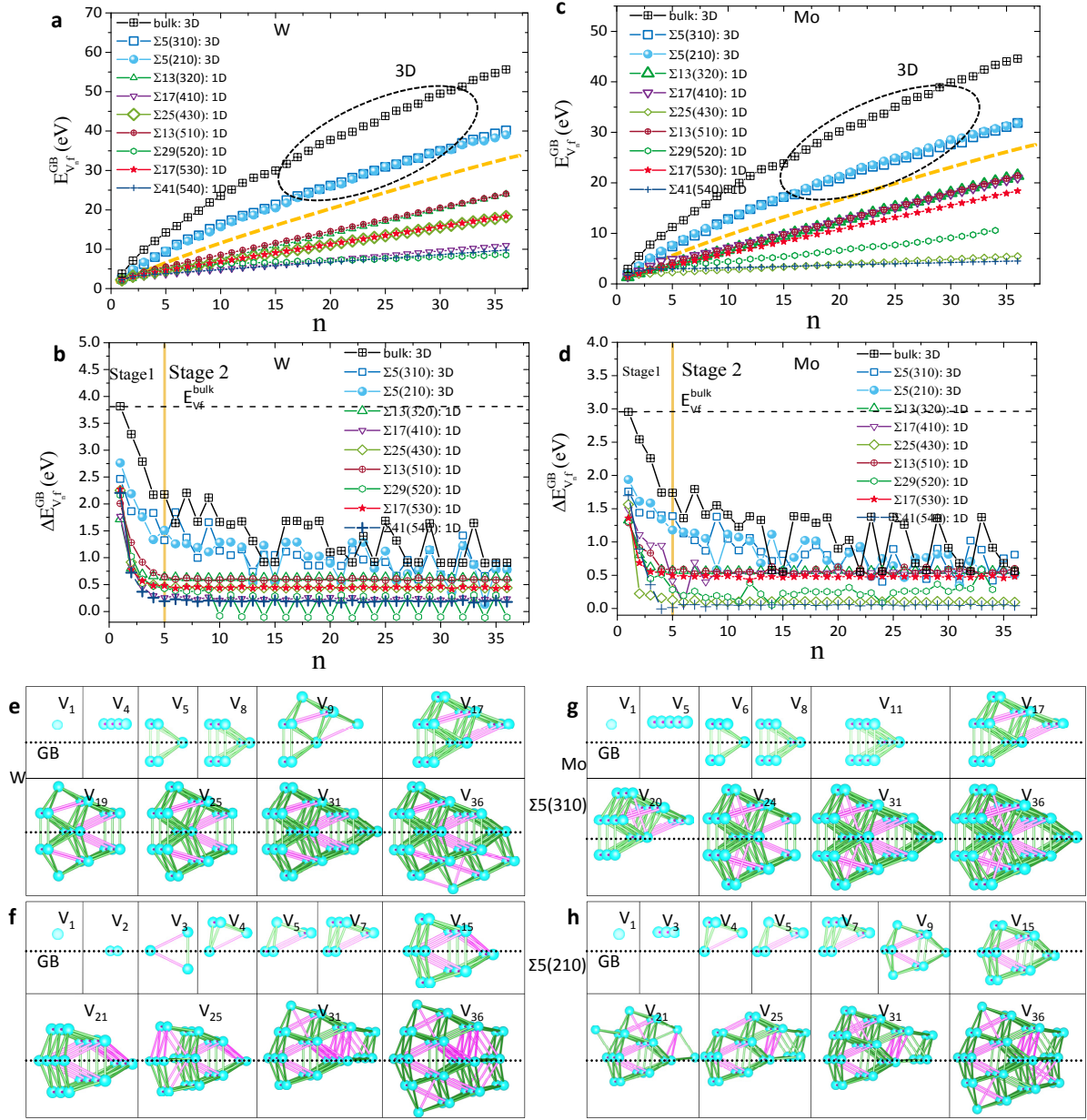


Fig. 4. (a) and (b) The formation energy for the vacancy cluster ($E_{V_n}^f$) and the differential energy ($\Delta E_{V_n}^f = E_{V_{n+1}}^f - E_{V_n}^f$) as a function of n for several W GBs. (c) and (d) The $E_{V_n}^f$ and $\Delta E_{V_n}^f$ as a function of n for several Mo GBs. For comparison, the energetic results for bulk V_n in W/Mo are also shown. (e) and (f) The groundstate configurations of typical V_n s in W GBs of $\Sigma 5(310)/[001]$ and $\Sigma 5(210)/[001]$, respectively. (g) and (h) The groundstate configurations of typical V_n s in Mo GBs of $\Sigma 5(310)/[001]$ and $\Sigma 5(210)/[001]$, respectively. In (e–h), the V in a V_n is represented by a cyan sphere. The first and second nearest V of a V is connected by a green and pink line, respectively.

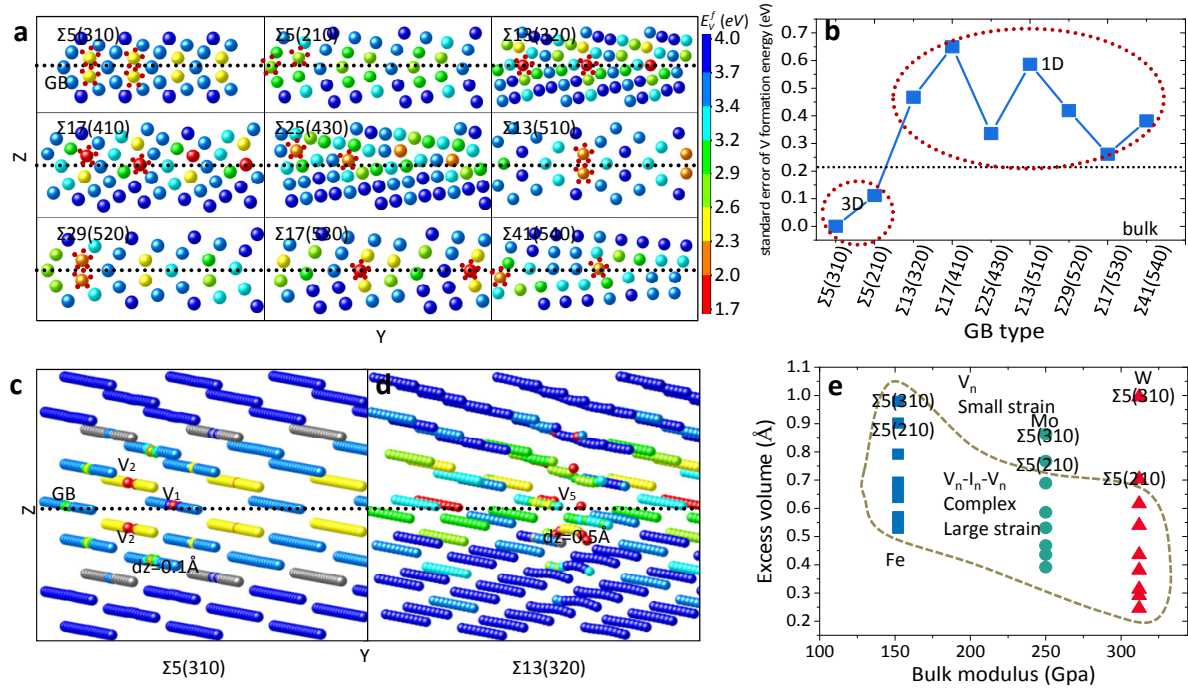


Fig. 5. (a) The distribution of vacancy formation energy within several W GBs. (b) Standard error of vacancy formation energy (E_V^f) for the group of GB atoms with low E_V^f as a function of the GB type in W. (c) and (d) The structure of a three-dimensional (3D) and 1D vacancy cluster at the W GB of $\Sigma 5(310)$ and $\Sigma 13(320)$, respectively. (e) Relation of the V_n configuration within the investigated Fe/Mo/W GBs with the GB excess volume and the bulk modulus of Fe/Mo/W.

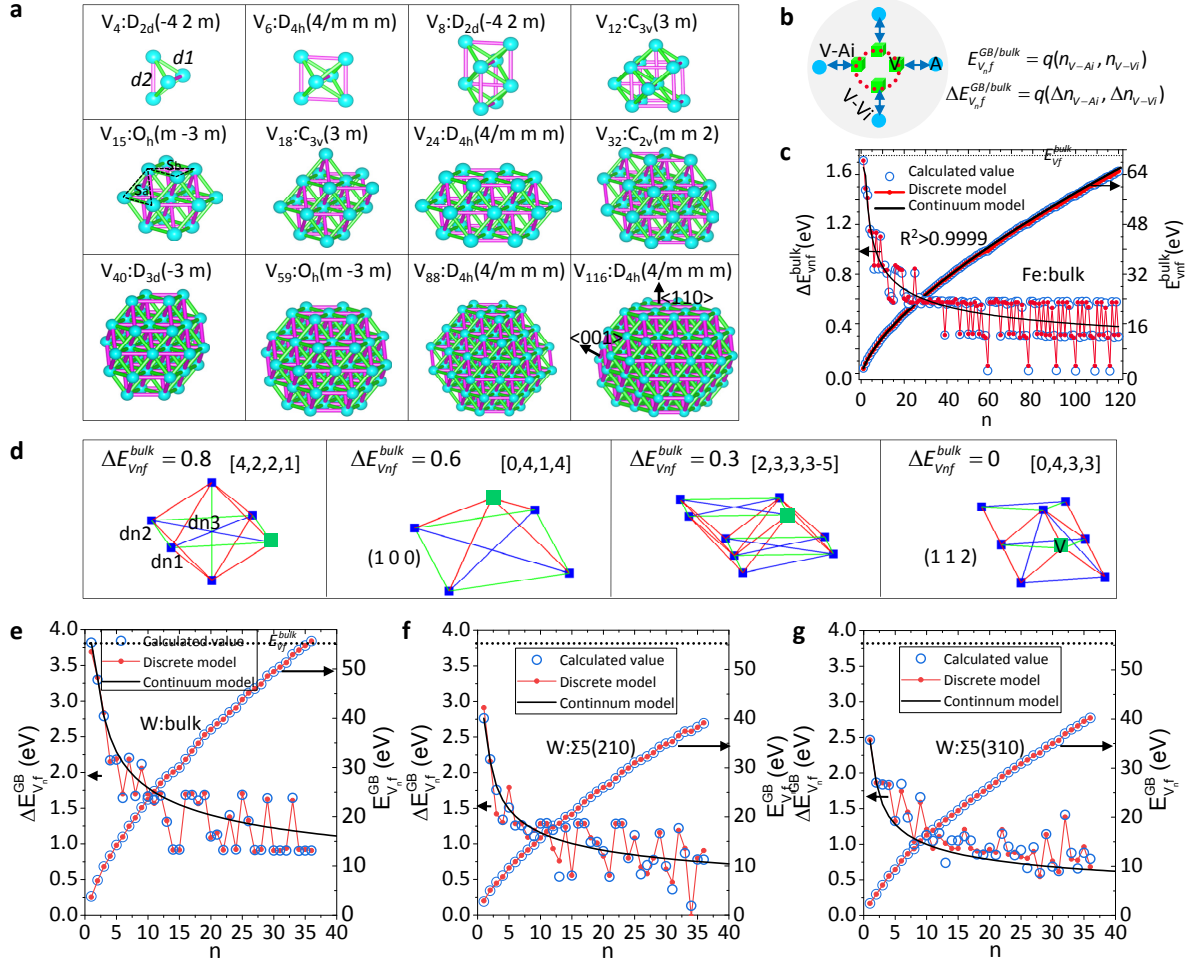


Fig. 6. (a) The groundstate configurations of typical V_n s in Fe bulk. Here, the V in a V_n is represented by a cyan sphere. The first and second nearest V of a V is connected by a green and pink line, respectively, while $d1$ and $d2$ marked near V_4 denotes the respective neighboring distance. **(b)** The local atomic environment for a V_n described by its neighboring atom (Ai), neighboring vacancy (Vi). Here, n_{V-Ai} , n_{V-Vi} denotes the number of V-Ai, V-Vi, respectively. $q(n_{V-Ai}, n_{V-Vi})$ and $q(\Delta n_{V-Ai}, \Delta n_{V-Vi})$ denotes the linear combination of n_{V-Ai} , n_{V-Vi} and Δn_{V-Ai} , Δn_{V-Vi} , respectively. The green cubic and blue sphere represents a vacancy and its neighboring atom. **(c)** The formation energy for the vacancy cluster ($E_{V_n}^f$) and the differential energy ($\Delta E_{V_n}^f = E_{V_{n+1}}^f - E_{V_n}^f$) as a function of n for bulk Fe. **(d)** The relation of the V energy level to the local atomic environment. The first, second and third nearest neighbor of the V is respectively connected by the red, green and blue line, respectively. The green cubic indicates the V added on a V_n . **(e-g)** Model prediction of $E_{V_n}^f$ and $\Delta E_{V_n}^f$ in W bulk, and GBs of $\Sigma(2\ 1\ 0)/[0\ 0\ 1]$ and $\Sigma(3\ 1\ 0)/[0\ 0\ 1]$, respectively.

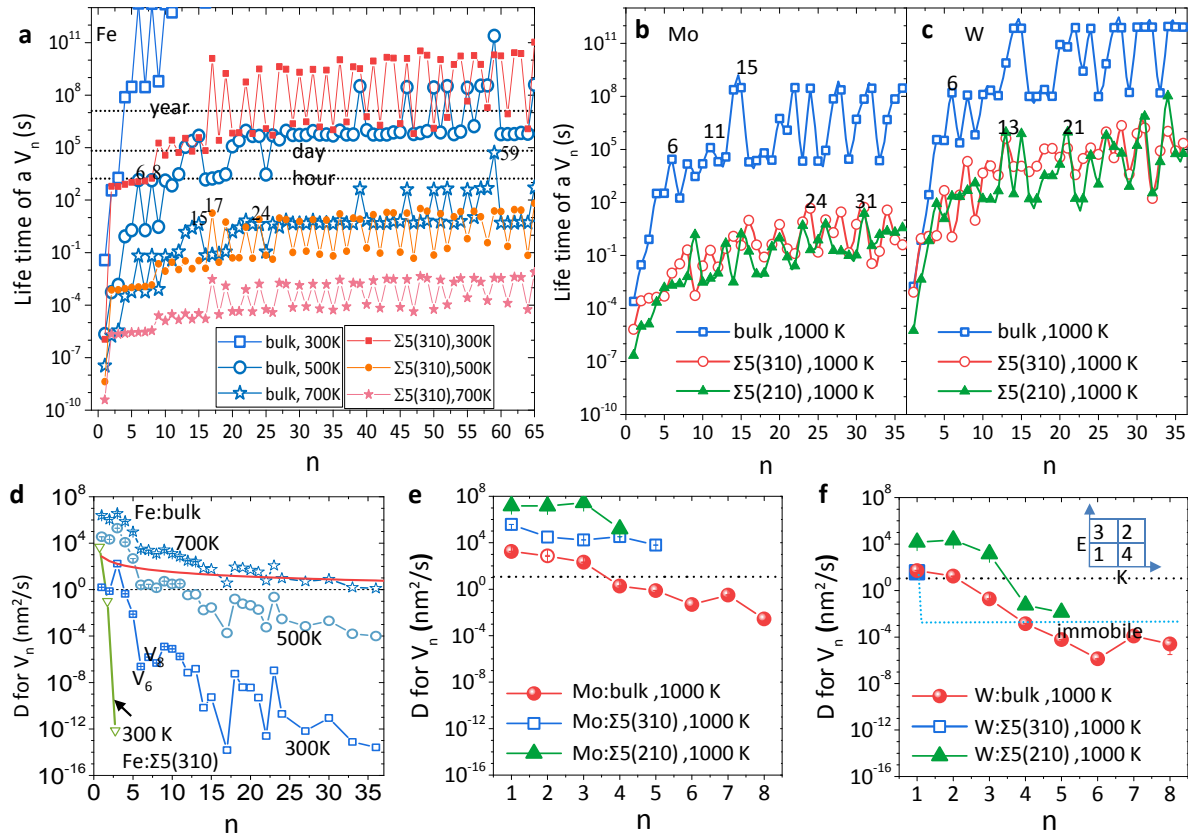


Fig. 7. (a–c) The lifetime of a V_n at several typical temperatures as a function of n . (d–f) Diffusion coefficients for small V_n within Fe/Mo/W GBs of $\Sigma 5(3\ 1\ 0)/[0\ 0\ 1]$ and $\Sigma 5(2\ 1\ 0)/[0\ 0\ 1]$. For comparison, bulk values for V_n are also presented. In the inset figure of (f), E and K denotes the thermal and kinetic stability, respectively of a V_n .

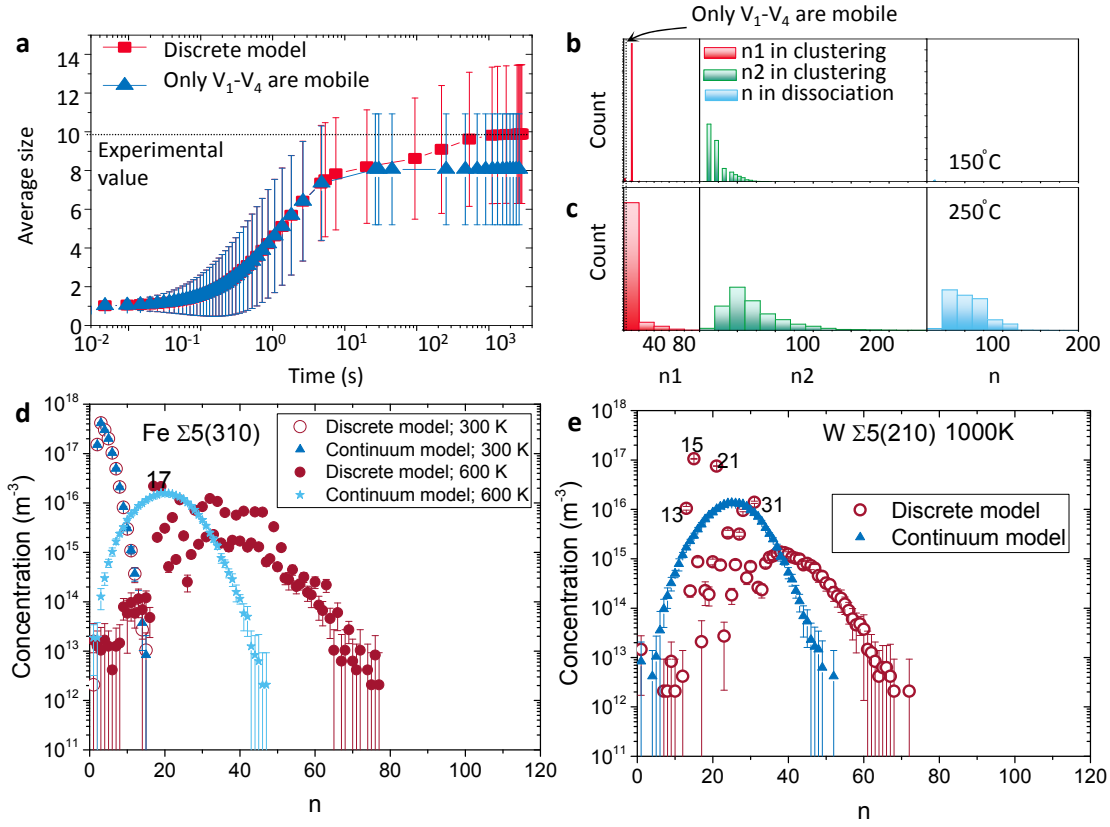


Fig. 8. (a) The average size of the V_n during annealing a Fe bulk system that initially contains a concentration of $5 \times 10^{25} m^{-3}$ of single vacancies for 50 minutes at temperature of 50°C. (b) and (c) The distribution of the size of V_n entering into the clustering and dissociation reaction at 150 and 250°C, respectively. (d) and (e) The cluster density distribution after annealing a system that initially contains a concentration of $5 \times 10^{18} m^{-2}$ of single vacancies for 50 minutes for Fe GB of $\Sigma 5(310)/[001]$ and W GB of $\Sigma 5(210)/[001]$, respectively.

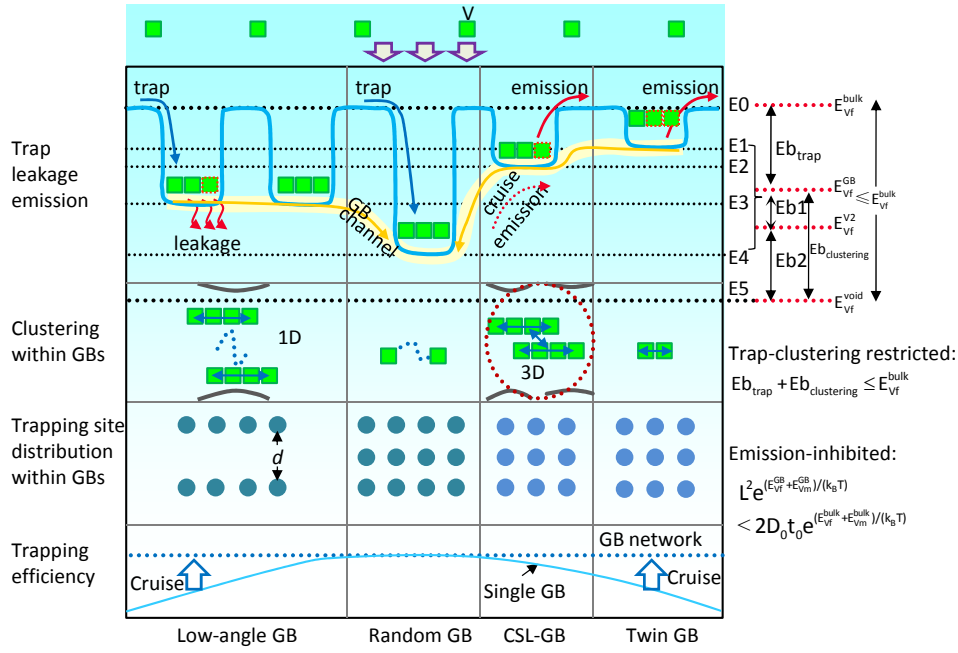


Fig. 9. Illustration of the defects trapping and clustering at a single GB and a GB network. The symbols $E0-E5$ denote the V energy level at different GBs. $E_{b_{\text{trap}}}$ is for the V-GB binding energy. E_{b1} is for the V-V binding energy at the GB, while E_{b2} is for the binding energy of the V with a GB void. The inequality of $E_{b_{\text{trap}}} + E_{b_{\text{clustering}}} \leq E_{\text{Vf}}^{\text{bulk}}$ describes the restricted relation of the V-GB binding energy to the energetic driving force for the V-clustering at the GB. The gray bow-shaped curve around a void indicates the compressive strain near the GB void. The inequality of $L^2 e^{(E_{\text{Vf}}^{\text{GB}} + E_{\text{Vm}}^{\text{GB}})/(k_B T)} < 2D_0 t_0 e^{(E_{\text{Vf}}^{\text{bulk}} + E_{\text{Vm}}^{\text{bulk}})/(k_B T)}$ describes the coupling condition of the grain size (L) and in-boundary V formation and migration when the emission of the V is inhibited due to the cruise of the V along the GB to find a low energy site. Here, $E_{\text{Vf}}^{\text{GB}}$ and $E_{\text{Vm}}^{\text{GB}}$ denotes the vacancy formation energy and migration energy barrier at the GB, respectively, while $E_{\text{Vf}}^{\text{bulk}}$ and $E_{\text{Vm}}^{\text{bulk}}$ is the corresponding value for a bulk V. D_0 and t_0 is the pre-exponential factor for vacancy diffusion coefficient and emission time at the GB, respectively. Here, $D_0 t_0 = d_m^2$ with d_m as jump distance of the V at the GB. T is absolute temperature and k_B is Boltzmann constant.